












Sub-millisecond conformational dynamics of the A_{2A} adenosine receptor revealed by single-molecule FRET

Ivan Maslov ^{1,2,3}, Oleksandr Volkov ¹³, Polina Khorn ¹, Philipp Orekhov ⁴, Anastasiia Gusach^{1,11}, Pavel Kuzmichev¹, Andrey Gerasimov^{1,5}, Aleksandra Luginina ¹, Quinten Coucke ³, Andrey Bogorodskiy¹, Valentin Gordeliy⁶, Simon Wanninger ⁷, Anders Barth ^{7,12}, Alexey Mishin¹, Johan Hofkens^{3,8}, Vadim Cherezov ⁹, Thomas Gensch³, Jelle Hendrix ^{2,3}✉ & Valentin Borshchevskiy ^{1,10}✉

The complex pharmacology of G-protein-coupled receptors (GPCRs) is defined by their multi-state conformational dynamics. Single-molecule Förster Resonance Energy Transfer (smFRET) is well suited to quantify dynamics for individual protein molecules; however, its application to GPCRs is challenging. Therefore, smFRET has been limited to studies of inter-receptor interactions in cellular membranes and receptors in detergent environments. Here, we performed smFRET experiments on functionally active human A_{2A} adenosine receptor (A_{2A}AR) molecules embedded in freely diffusing lipid nanodiscs to study their intramolecular conformational dynamics. We propose a dynamic model of A_{2A}AR activation that involves a slow (>2 ms) exchange between the active-like and inactive-like conformations in both apo and antagonist-bound A_{2A}AR, explaining the receptor's constitutive activity. For the agonist-bound A_{2A}AR, we detected faster (390 ± 80 μs) ligand efficacy-dependent dynamics. Our work establishes a general smFRET platform for GPCR investigations that can potentially be used for drug screening and/or mechanism-of-action studies.

¹Research Center for Molecular Mechanisms of Aging and Age-Related Diseases, Moscow Institute of Physics and Technology, Dolgoprudny Moscow Region, Russia. ²Dynamic Bioimaging Lab, Advanced Optical Microscopy Centre, Biomedical Research Institute, Agoralaan C (BIOMED), Hasselt University, Diepenbeek, Belgium. ³Laboratory for Photochemistry and Spectroscopy, Division for Molecular Imaging and Photonics, Department of Chemistry, KU Leuven Leuven, Belgium. ⁴Faculty of Biology, Shenzhen MSU-BIT University, Shenzhen, China. ⁵Vyatka State University, Kirov, Russia. ⁶Institut de Biologie Structurale J.-P. Ebel, Université Grenoble Alpes-CEA-CNRS, Grenoble, France. ⁷Physical Chemistry, Department of Chemistry, Center for Nano Science (CENS), Center for Integrated Protein Science (CIPSM) and Nanosystems Initiative München (NIM), Ludwig-Maximilians-Universität München, Munich, Germany. ⁸Max Planck Institute for Polymer Research, Mainz, Germany. ⁹Bridge Institute, Department of Chemistry, University of Southern California, Los Angeles, CA, USA. ¹⁰Joint Institute for Nuclear Research, Dubna, Russian Federation. ¹¹Present address: MRC Laboratory of Molecular Biology, Cambridge, UK. ¹²Present address: Department of Bionanoscience, Kavli Institute of Nanoscience, Delft University of Technology, HZ Delft, The Netherlands. ¹³Unaffiliated. ✉email: jelle.hendrix@uhasselt.be; borshchevskiy.vi@phystech.edu

G-protein-coupled receptors (GPCRs) constitute the largest superfamily of membrane proteins in humans containing over 800 members, which mediate critical physiological processes, such as neurotransmission, homeostasis, inflammation, reproduction, olfaction, vision, taste, and others^{1,2}. GPCRs recognize a large variety of endogenous extracellular signaling molecules transmitting their corresponding signals inside the cell, and this process can be modulated by synthetic ligands or drug molecules. In fact, over 30% of all FDA-approved drugs target GPCRs³. Multiple lines of evidence suggest that the molecular mechanism of GPCR activation extends beyond a simple “on/off” mode. First, apo receptors show basal activity that can be suppressed by inverse agonists⁴. Second, different agonists vary in efficacy and can stimulate receptor activity to a different extent⁵. Third, a single receptor can signal through several intracellular pathways, some of which could be preferentially activated by so-called “biased” ligands⁶. These three phenomena indicate that receptors are highly dynamic molecules and sample several active and inactive states stochastically (for review, see refs. 7–9).

The A_{2A} adenosine receptor ($A_{2A}AR$) is expressed in many organs and tissues including those in the immune system, basal ganglia, heart, lungs, and blood vessels¹⁰. Throughout the body, $A_{2A}AR$ regulates the cardiovascular tonus causing vasodilation and promotes healing of inflammation-induced injuries by suppressing immune cells^{11,12}. In the brain, $A_{2A}AR$ modulates dopamine and glutamate neurotransmission¹². $A_{2A}AR$ is a promising target for drugs against insomnia, chronic pain, depression, Parkinson’s disease, and cancer^{12,13}. On the molecular level, $A_{2A}AR$ is activated by the endogenous extracellular agonist adenosine and initiates the cAMP-dependent signaling pathway via G_s and G_{olf} proteins^{12,14}. Besides G proteins, $A_{2A}AR$ interacts with numerous other partners including GRK-2 kinase, β -arrestin, and other GPCRs^{14,15}. One cryoEM and over 50 high-resolution X-ray crystallographic structures are available for antagonist- or agonist-bound $A_{2A}AR$ and for its ternary complex with an agonist and an engineered G protein, making this receptor an excellent model system for investigating GPCR structural dynamics. While static structures provide critical information about the receptor’s lowest energy states, our understanding of the $A_{2A}AR$ function remains critically incomplete without detailed knowledge of its conformational dynamics.

The current information about $A_{2A}AR$ conformational dynamics is based mostly on several reported NMR experiments^{16–24}. In response to ligand binding, different $A_{2A}AR$ amino acids either alter their sole stable conformations or vary relative probabilities of coexisting stable conformations^{16,17}. On the picosecond-to-nanosecond timescale, some $A_{2A}AR$ amino acids increase side-chain dynamics, while others become stabilized¹⁸. Sub-millisecond conformational variability was shown for both apo-form¹⁹ and agonist-bound $A_{2A}AR$ ^{16,17,20}. Large-scale conformational changes in $A_{2A}AR$ with dwell times of seconds were also reported^{19,21}, but two independent studies described the corresponding long-lived states differently: in one report¹⁹, a 3-state model with an attributed basal activity of 70% was proposed, while in the other²¹, the authors put forward a 4-state model with a negligible basal activity. Thus, the current picture of $A_{2A}AR$ dynamics is complex and contradictory.

Studies of $A_{2A}AR$ dynamics face two major challenges: first, the need to cover a wide range of timescales from nanoseconds to seconds, and next, the difficulty to untangle multiple protein states within the ensemble. Single-molecule fluorescence spectroscopy provides tools to address both of these difficulties. Depending on the applied method, the fluorescence signal from individual receptors can be tracked with as low as a nanosecond temporal resolution for a total duration of either millisecond in case of freely diffusing molecules or even seconds to minutes using immobilized molecules^{7,25}.

Single-molecule fluorescence spectroscopy methods have been previously applied to study GPCR conformational dynamics⁷. For example, environmentally sensitive fluorescent dyes have been used as single-molecule reporters of conformational changes in the β_2 adrenergic receptor (β_2AR)^{26–29}, visual rhodopsin^{30,31}, and, more recently, $A_{2A}AR$ ³². Single-label experiments are attractive because of a minimal influence of the dye on the native receptor dynamics, but the experimental readouts are often limited and lack detailed structural interpretation. In addition, the results of single-label experiments can be obscured by multi-state dye photophysics. Another approach, based on single-molecule Förster Resonance Energy Transfer (smFRET) between two dyes can provide more direct structural outcomes and introduce additional internal controls, however, at the expense of double-labeling. smFRET has been shown to be especially useful to investigate structural dynamics of GPCR dimers^{33–37}. To our knowledge, at the moment of this writing, ref. 38 is the only published application of smFRET to quantifying intramolecular conformational dynamics in GPCRs; this study addressed structural changes on the intracellular side of immobilized β_2AR in detergent micelles.

Here, we applied smFRET to investigate the conformational dynamics of $A_{2A}AR$ in lipid nanodiscs freely diffusing in solution without immobilization. Using the MFD-PIE (multiparameter fluorescence detection with pulsed-interleaved excitation) technique³⁹ (Fig. 1a), we tracked the relative movements of two dyes attached to the intracellular tip of the transmembrane helix TM6 (L225C^{6,27}, superscripts indicate Ballesteros-Weinstein numbering⁴⁰) and to the C-terminal intracellular helix H8 (Q310C^{8,65}) of $A_{2A}AR$ (Fig. 1b). We observed that FRET efficiency in the double-labeled $A_{2A}AR$ increases upon agonist binding (Fig. 1c). Several burst-wise fluorescence analysis approaches—plot of burst-wise FRET efficiency against donor fluorescence lifetime⁴¹, FRET 2-Channel kernel-based Density Estimator (FRET-2CDE)⁴², Burst Variance Analysis (BVA)⁴³, and filtered Fluorescence Correlation Spectroscopy (fFCS)⁴⁴—subsequently revealed sub-millisecond conformational dynamics of $A_{2A}AR$. Based on quantitative analysis of the obtained data for the receptor in its apo-state and upon addition of the inverse agonist ZM241385, the partial agonist LUF5834, or the full agonist NECA to the receptor, we finally propose a dynamic model of $A_{2A}AR$ activation.

Results

Labeling and reconstitution of $A_{2A}AR$ in nanodiscs. To track the conformational dynamics of $A_{2A}AR$ with smFRET we chose to attach two fluorescent dyes to mutated residues L225C^{6,27} on the intracellular end of TM6 and Q310C^{8,65} on the C-terminal end of H8 (Fig. 1b and Supplementary Fig. 1a). In previous $A_{2A}AR$ FRET studies, a fluorescent protein-based FRET donor and fluorescent molecule based acceptor in similar labeling positions were shown to provide sufficient contrast between the active and inactive receptor states in live cells^{45,46}. The L225C^{6,27} position is also homologous to the native cysteine C265^{6,27} in β_2AR that has been frequently used for fluorescent labeling^{26–28,47–51}.

We expressed the double-Cys mutant (L225C^{6,27}/Q310C^{8,65}) of $A_{2A}AR$ in *Leishmania tarentolae* and simultaneously labeled it with two maleimide-functionalized dyes, Alexa488 and Atto643 (“Protein expression, purification and labeling” in “Methods”). The wild-type (WT) $A_{2A}AR$ has six unpaired cysteines in its transmembrane helices (Supplementary Fig. 1a). To achieve specific labeling of the two genetically introduced cysteines, but spare the transmembrane native cysteines, we labeled the receptors in isolated cell membranes, as described previously⁵².

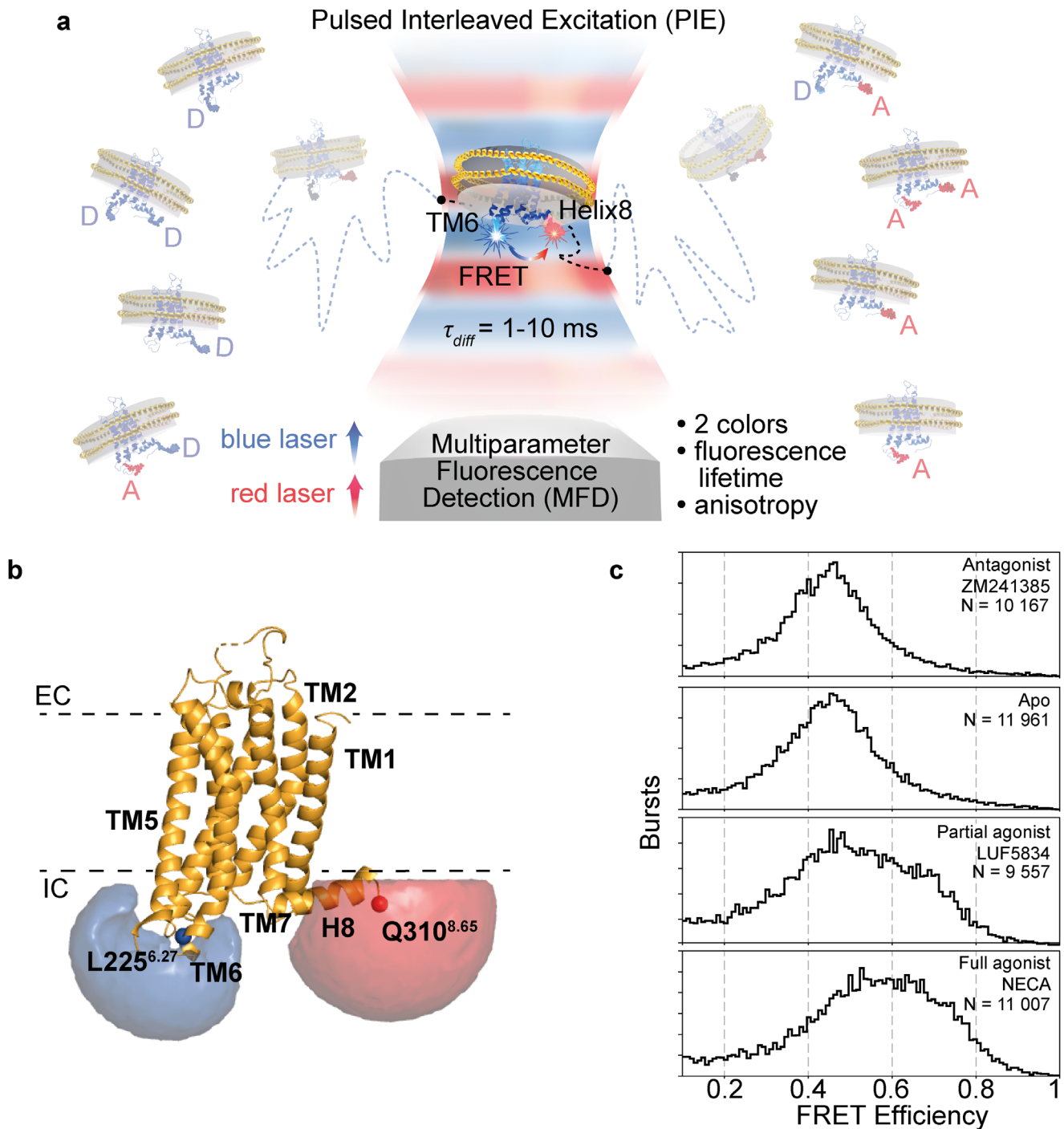


Fig. 1 Agonist-induced conformational changes in $A_{2A}AR$ are revealed by smFRET. **a** Schematic illustration of the MFD-PIE smFRET experiment on $A_{2A}AR$ embedded in lipid nanodiscs and stochastically labeled with the donor (Alexa488) and the acceptor (Atto643) fluorescent dyes at TM6 and H8. Eight coexisting labeling variants of $A_{2A}AR$ are shown as shadowed receptors in both sides of the image, “D” and “A” correspond to donor and acceptor dyes, respectively. $A_{2A}AR$ s diffuse in solution and stochastically cross the focal spot of an inverted fluorescence microscope. Bursts of fluorescence from donor and acceptor fluorophores are recorded within the 1-10 ms residence time of individual $A_{2A}AR$ s crossing the focal spot. Only those receptors labeled with both, donor and acceptor, produce FRET signal. In the PIE approach, two spatially overlapped and alternately pulsing lasers are focused by the microscope objective to excite donor and acceptor fluorescence consecutively. Using the MFD approach, fluorescence signals of the donor and acceptor are recorded separately, and the fluorescence lifetime and anisotropy of each dye are determined. **b** The labeled sites (L225^{6.27}, Q310^{8.65}) and the volume accessible for the dyes (simulated using FPS software¹⁰⁶) are shown on the $A_{2A}AR$ structure (PDB: 3EML⁶⁹), the extracellular (EC) and intracellular (IC) membrane boundaries are obtained from the PPM web server¹⁰⁷ and shown as dashed lines. **c** Burst-wise distributions show an agonist-induced increase in FRET efficiency in the double-labeled $A_{2A}AR$. The number of bursts used for the analysis (N) is given for each condition.

After labeling, the receptors were purified and reconstituted in MSP1D1 nanodiscs, which can accommodate only a single monomeric receptor per nanodisc (“Nanodisc reconstitution” in “Methods”)⁵³.

Size-exclusion chromatography confirmed a high purity and monodispersity of the nanodisc-reconstituted A_{2A}AR samples (Supplementary Fig. 1b). Labeling specificity was confirmed with the WT receptor, which showed only a marginal dye fluorescence associated with the protein after the labeling procedure (Supplementary Fig. 1b and Supplementary Table 1). In both ensemble spectra and lifetime measurements of the fluorescently labeled A_{2A}AR FRET-sensitized acceptor emission was readily observed, proving the existence of double-labeled FRET-active molecules in the samples (Supplementary Fig. 1c, d, “Fluorescence spectra characterization” and “Ensemble-based fluorescence lifetime measurements” in “Methods”).

To test whether the double-cysteine mutant A_{2A}AR (L225C^{6.27}/Q310C^{8.65}) is functional, we measured the ligand-induced thermostabilization of the isolated receptors as well as the agonist-induced cAMP accumulation in living cells. A fluorescent thermal stability assay⁵⁴ showed that the addition of either the antagonist ZM241385 or the agonist NECA in saturating concentrations increased the melting temperature of both WT and mutant A_{2A}AR with respect to the apo-state by >7 °C, indicating ligand-binding activity of the receptor (Supplementary Fig. 1e, “Thermal shift assay” in “Methods”). A BRET assay of cAMP accumulation in HEK293T cells transiently expressing A_{2A}AR showed very similar pEC₅₀ values (mean ± SD, three biological replicas) for both WT (6.41 ± 0.15) and double-mutant (6.45 ± 0.06) forms of the receptor upon stimulation with the agonist NECA (Supplementary Fig. 1f, “Measurement of A_{2A}AR surface expression and Gs-signaling” in “Methods”). Although several previous studies reported an order of magnitude higher potency of NECA against WT A_{2A}AR in CHO cells^{55–57}, pEC₅₀ values similar to those obtained here were measured in yeasts⁵⁸ and in membrane pellets isolated from CHO cells⁵⁹. The mutant form of A_{2A}AR retained ligand-binding activity in nanodiscs and signaling activity in HEK293T cells, therefore we assume that the conformational dynamics observed for the double-labeled receptor in smFRET experiments represent the native dynamics of the WT receptor.

smFRET reveals ligand-induced conformational changes in A_{2A}AR.

We diluted fluorescently labeled A_{2A}AR to nanomolar concentrations, mounted the sample on a microscope cover slip and recorded fluorescence intensity, lifetime, and anisotropy data from individual molecules diffusing freely across the femtoliter-sized observation spot (approximated by a 3D Gaussian with half-widths 0.5 μm, 0.5 μm and 2 μm) of a confocal fluorescence microscope (Fig. 1a, “Confocal MFD-PIE setup” and “smFRET data recording” in “Methods”). Inside the spot, donor and acceptor fluorophores are excited alternately using a two-color pulsed-interleaved excitation (PIE)⁶⁰. The residence time of individual molecules (~1–10 ms) in the laser spot sets the upper limit of timescales approachable for the observation of A_{2A}AR conformational dynamics. Using a 4-detector MFD scheme (Supplementary Fig. 2), photons detected from individual molecules were digitally tagged with (1) the spectral band in which they were detected, (2) their global arrival time with microsecond accuracy, (3) their relative arrival time with respect to the laser pulses within a ps-ns range, and (4) their optical polarization⁶¹. PIE, together with two-color detection, allowed us to distinguish double-labeled receptors (simultaneously labeled with donor and acceptor) from “donor-only” and “acceptor-only” receptors (Supplementary Fig. 3, “Burst identification” and “Selection of

double-labeled, donor-only and acceptor-only subpopulations” in “Methods”).

The fraction of A_{2A}ARs simultaneously labeled with donor and acceptor fluorophores showed different distributions of FRET efficiency depending on the bound ligand (Fig. 1c, “FRET efficiency and Stoichiometry” and “Correction factors” in “Methods”). The antagonist ZM241385 did not change FRET efficiency distribution within experimental error. On the contrary, both the partial agonist LUF5834 and the full agonist NECA shifted the mean FRET efficiency to larger values and increased the overall distribution width, compared to the apo-receptor. The increase in FRET efficiency was less pronounced for the partial agonist LUF5834 than for the full agonist NECA.

Fluorescence lifetime data suggest sub-millisecond conformational dynamics of A_{2A}AR. Besides fluorescence intensity, FRET is also reflected in fluorescence lifetime data. A two-dimensional plot of the per-burst FRET efficiency against the donor fluorescence lifetime provided the insights into the receptor’s conformational dynamics (Fig. 2a, b, “Burst-wise fluorescence lifetime” in “Methods”). In theory, data for rigid molecules, in which FRET efficiency remains constant over the duration of a burst should be distributed along a curved diagonal line that intersects the lifetime axis at the lifetime of the donor-only population and the FRET efficiency axis at unity, commonly referred to as the “static FRET line” (Fig. 2a). Alternatively, if receptor molecules sample different conformations during their residence time in the focal spot (1–10 ms) on a timescale that is longer than the nanosecond fluorescence lifetime, their bursts should be shifted from the “static FRET line” toward the longer lifetime region. This phenomenon can be explained by the higher weights of the lower FRET states in the fluorescence lifetime averaging due to the larger number of photons emitted by the donor. The observed rightward deviations of our burst data from the static FRET line are statistically significant and indicate the existence of sub-millisecond conformational dynamics (beyond the fast dynamics expected for dye linkers) in the apo as well as agonist- and antagonist-bound states of A_{2A}AR (Fig. 2b and Supplementary Fig. 4).

FRET-2CDE and BVA confirm that agonists enhance conformational dynamics in A_{2A}AR compared to apo-receptor.

Variations of FRET efficiency within fluorescence bursts from individual receptors suggest the presence of conformational dynamics. To analyze these variations further we used two complementary approaches: FRET-2CDE⁴² and BVA⁴³. Both methods assign dynamics scores to individual molecules and are sensitive to the dynamics that are slower than the time used for FRET efficiency averaging (roughly 100 μs for both approaches).

The FRET-2CDE score provides an unbiased way for the separation of static and dynamic subpopulations of molecules and for the comparison of their fractions in different datasets⁴² (“FRET-2CDE analysis” in “Methods”). The main advantage of FRET-2CDE is that it is minimally influenced by the mean FRET efficiency in a dynamic molecule. Theoretically, static molecules should have FRET-2CDE ≈ 10, while higher FRET-2CDE values correspond to more pronounced conformational dynamics (Fig. 2c). In our data, neither the apo nor ligand-bound A_{2A}AR showed a clear separation of different receptor subpopulations along the FRET-2CDE axis, but the observed deviations of FRET-2CDE scores from those expected for fully static molecules were statistically significant (Supplementary Fig. 5). In addition, agonists increased the mean FRET-2CDE score of A_{2A}AR compared to the apo or antagonist-bound receptors (Supplementary Table 2). The fraction of receptors that exceeded the

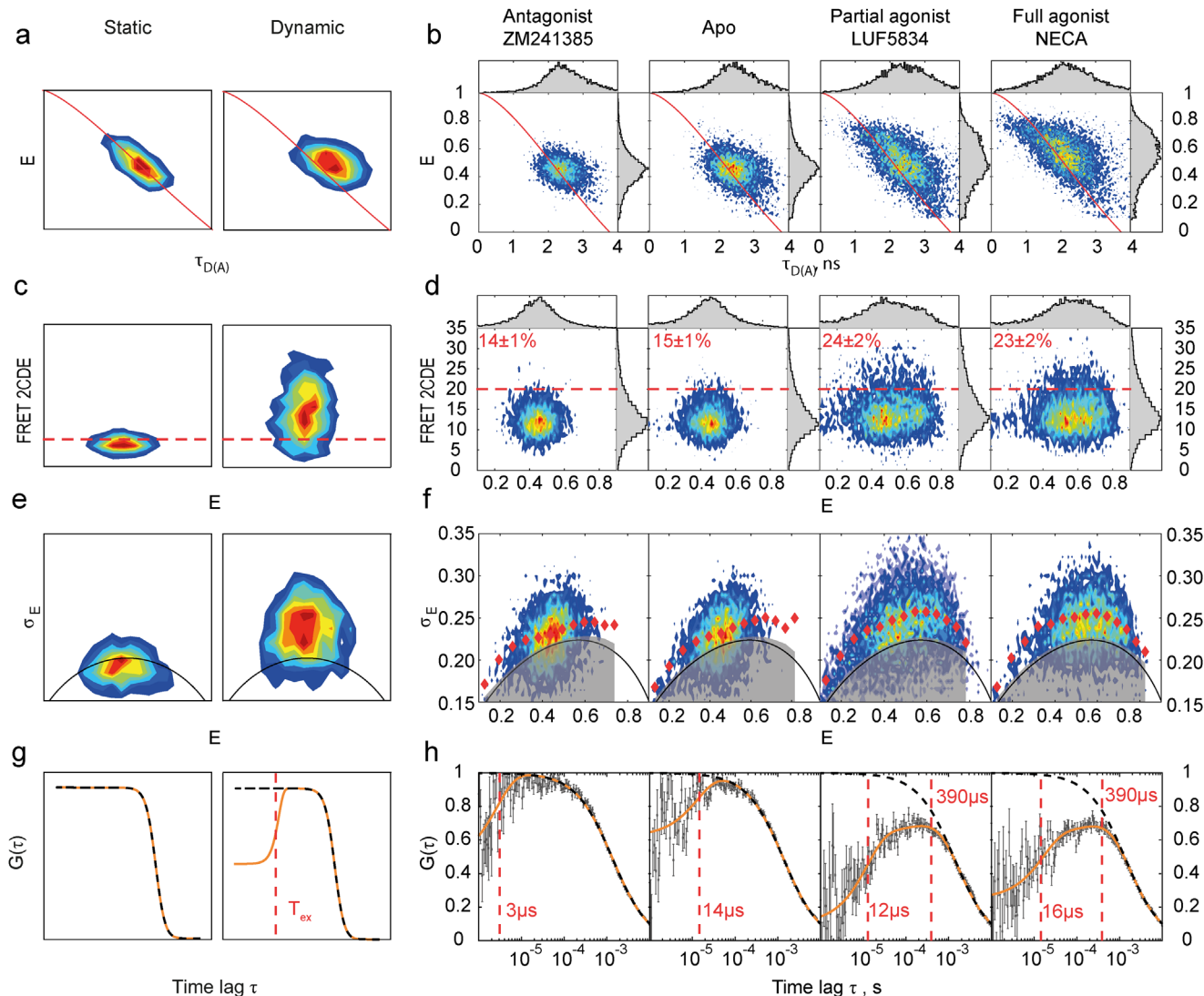


Fig. 2 Four complementary burst-wise analysis approaches suggest an agonist-induced increase in the sub-millisecond conformational dynamics of $A_{2A}AR$. Contour plots are two-dimensional histograms of different fluorescence burst parameter distributions. The qualitative differences between “static” and “dynamic” molecules expected in each analysis approach are shown in the drawings (**a**, **c**, **e**, **g**). The experimental data for double-labeled $A_{2A}AR$ are shown in the plots (**b**, **d**, **f**, **h**). **a**, **b** The FRET efficiency is plotted against donor fluorescence lifetime. The ‘static FRET’ line is shown in red. A shift of burst distribution to the right from the red line indicates dynamic FRET. **c**, **d** The FRET-2CDE dynamics score is plotted against FRET efficiency E . The FRET-2CDE = 20 threshold is indicated as red dashed lines, and the percentage of bursts with FRET-2CDE > 20 is shown in red text (mean \pm SD, three technical replicas with different protein aliquots). **e**, **f** BVA dynamics scores are plotted against FRET efficiency. Red diamonds show the centers of burst subgroups equally spaced along the FRET efficiency axis. The solid black lines show mean BVA scores, and the transparent gray areas demonstrate 99.9% confidence intervals expected for static molecules, given the shot noise present in the data. **g**, **h** The cross-correlation fFCS function is plotted against time lag. Experimental points with error bars are shown in gray; the error bars are SDs obtained after splitting the photon data into ten equally sized bins and correlating each individually. The fitting curves are shown in orange; the diffusion-related terms are shown as dashed black lines; the exchange times derived from the fit are highlighted with vertical red lines. χ_{red}^2 of the global fit is 1.1. The source data is available online as Supplementary Data 1. The number of fluorescence bursts used for the analysis are the same as for Fig. 1c: 10,167 for ZM241385, 11,961 for apo-state, 9557 for LUF5834, 11,007 for NECA.

threshold FRET-2CDE > 20 was also higher for the agonist-bound receptors: $14 \pm 1\%$ for ZM241385, $15 \pm 1\%$ for apo, $24 \pm 2\%$ for LUF5834, $23 \pm 2\%$ for NECA (Fig. 2d). The fraction of molecules with high-FRET-2CDE scores is larger for the agonist-bound receptor for any threshold value (Supplementary Fig. 6). These results indicate that either the amplitude of the observed dynamics or the number of the inter-state transitions per burst increase in $A_{2A}AR$ upon agonist binding.

BVA provides a statistically robust way to test whether the observed variations of FRET efficiency exceed fluctuations expected from the shot noise and thus to prove conformational

dynamics⁴³. To apply BVA, we split bursts into consecutive photon windows with $n = 5$ photons in each ($\sim 100 \mu s$ long), calculated standard deviations of the bin-wise FRET efficiencies within each burst, and plotted them against the mean FRET efficiency (“Burst Variance Analysis (BVA)” in “Methods”). The obtained BVA scores exceeded the 99.9% confidence interval expected from the shot noise under all four conditions (Fig. 2e, f), therefore, BVA confirmed that sub-millisecond conformational dynamics are already present in the apo and antagonist-bound $A_{2A}AR$ and further increased in the agonist-bound $A_{2A}AR$.

fFCS reveals fast photophysics-related dynamics and slow agonist-induced dynamics in A_{2A} AR. To estimate the timescales of A_{2A} AR conformational dynamics we applied the fFCS approach⁴⁴ (“Filtered Fluorescence Correlation Spectroscopy (fFCS)” in “Methods”). We used the photon arrival time and anisotropy information to split the photon stream from the double-labeled molecules in *silico* between the low-FRET (LF) and high-FRET (HF) channels (Supplementary Fig. 7). Theoretically, if the LF and HF species are just two extremes of a heterogeneous ensemble of long-lived receptor states, then cross-correlation between the two channels will show only a diffusion-based sigmoidal component decreasing with the correlation lag time (Fig. 2g). Contrarily, if the LF and HF species interconvert on the μ s–ms timescales, the cross-correlation should be lower in the time lag region shorter than the state exchange time (Fig. 2g). For all four conditions, fFCS curves deviate from the diffusion-related sigmoidal trend (Fig. 2h, Supplementary Data 1). For the apo and antagonist-bound receptor, the deviations (later called anticorrelations) are pronounced only in the 1–100 μ s timescale, while for the agonist-bound protein the anticorrelation is also apparent in the 100–1000 μ s timescale.

In the 1–100 μ s timescale, fFCS-anticorrelation is expected from donor and acceptor photobleaching, as was also evident in sub-ensemble FCS analyses of single-labeled molecules for all apo/ligand-bound conditions (Supplementary Fig. 8). Dynamics of the dye linkers and local fluctuations of protein structure may also contribute to anticorrelation at this fast timescale. In the 100–1000 μ s timescale, no dynamics were detected in sub-ensemble FCS for single-labeled molecules (Supplementary Fig. 8). This proves that the observed agonist-induced FRET dynamics are not due to dye photophysics, but must arise from sub-millisecond protein dynamics.

To quantify the exchange time of these dynamics, we fitted the anticorrelation terms in the fFCS curves with exponential decays. Initially, we employed just one anticorrelation term for each dataset, and optimized the diffusion time τ_{diff} globally across all four datasets. This fit adequately described the data for the apo/antagonist-bound A_{2A} AR, but showed systematic deviations in the 1–10 μ s region for the agonist-bound A_{2A} AR (Supplementary Fig. 9, Supplementary Table 3A, $\chi_{red}^2 = 1.5$). For this reason, we introduced a second anticorrelation term in the fitting model for the agonist-bound A_{2A} AR.

In this way, with one anticorrelating term for the apo and antagonist-bound A_{2A} AR and two anticorrelating terms for the agonist-bound receptor, we obtained a satisfactory fit (Fig. 2h and Supplementary Table 3B, $\chi_{red}^2 = 1.1$). The fast anticorrelation term (A_1) was present in all four datasets and was assigned mostly to dye photophysics; the slow anticorrelation term (A_2) appeared only in the agonist-bound receptor data. This fFCS model adequately describes the experimental data for all conditions and provides the exchange time of slow agonist-induced dynamics $\tau_2 = 390 \pm 80 \mu$ s (error was estimated as a half-width of the 95% confidence interval of the fitting).

PDA quantifies populations of active-like and inactive-like states in dynamic A_{2A} AR. To quantify the populations of A_{2A} AR in different FRET states in the apo and ligand-bound forms we used the photon distribution analysis (PDA) method^{62,63} (“Photon distribution analysis (PDA)” in “Methods”). In contrast to multi-state Gaussian fitting, PDA explicitly describes FRET data by taking into account the background, shot noise and receptor dynamics. For PDA, we split the fluorescence bursts into time bins of constant duration (0.5 ms, 1 ms, and 2 ms) and analyzed them globally across apo and ligand-bound conditions. In dynamic systems, a molecule can sample several states during

an individual time bin, and therefore, the FRET efficiency distribution depends on the duration of the time bin. PDA is most sensitive for picking up interconversion times on the diffusion timescale (1–10 ms); for faster or slower dynamics, PDA can, however, still be constrained a priori to demonstrate that the proposed model of the conformational space does not contradict the observed FRET efficiency distributions. All models with less than three states produced a poor fit of experimental data with $\chi_{red}^2 > 10$. The best among them was a model with two interconvertible states providing $\chi_{red}^2 = 10.3$ (Supplementary Fig. 10, Supplementary Table 4). Meanwhile, a three-state PDA model with three static states described the experimental distributions well ($\chi_{red}^2 = 3.2$, Supplementary Fig. 11 and Supplementary Table 5).

Despite the low χ_{red}^2 , the static three-state PDA model contradicts our findings from fFCS analyses, where fast dynamics were present in all apo/ligand-bound receptor forms and additional slow dynamics appeared in the agonist-bound A_{2A} AR. We, therefore, subsequently examined whether an fFCS-inspired model could equally well describe the experimental data in PDA. Since PDA is insensitive to fast (<20 μ s) dynamics observed in fFCS, the fitting model for the apo and antagonist-bound A_{2A} AR included only three static states. For the agonist-bound A_{2A} AR, we introduced a slow dynamics component with a fixed exchange time ($\tau_2 = 390 \pm 80 \mu$ s, as observed in fFCS) between two states, while keeping the third one static. This fFCS-constrained PDA model adequately described the experimental data ($\chi_{red}^2 = 3.6$, Fig. 3a, Supplementary Fig. 12, Supplementary Table 6, and Supplementary Data 2). The difference between χ_{red}^2 for the fully static and fFCS-constrained dynamic models (3.2 and 3.6, respectively) was insignificant within experimental error (“Photon distribution analysis (PDA)” in “Methods”). Together, both fFCS and PDA can thus be consistently described by the same unified kinetic model. We further used this model to quantify the populations of the A_{2A} AR states.

Using the fFCS-constrained model in PDA we determined the mean values and variances of the FRET efficiency and populations for each PDA state under the apo and ligand-bound conditions (Fig. 3a, Supplementary Fig. 12, and Supplementary Table 6). PDA converged to a model, where the static state exhibited the lowest FRET efficiency (LF) and the interconvertible states (MF and HF) possessed a medium and high-FRET efficiency, respectively. The PDA results (Fig. 3a) revealed that both agonists increased the population of the highest FRET efficiency state (HF state), and decreased the population of the state with intermediate FRET efficiency (MF) state—therefore, we assume that the HF and MF states correspond to the active-like and inactive-like conformations of A_{2A} AR, respectively. Approximately 10–20% of A_{2A} AR molecules always stay in the low-FRET (LF) state independently of the added ligand—we assign this fraction to receptors locked in a long-lived non-functional state or improperly folded protein.

Interestingly, the active-like HF state is also observed in the apo-receptor ensemble and even in the ZM241385-bound receptors. Additionally, the sample with the full agonist NECA has a higher population of the active-like HF state compared to the partial agonist LUF5834. The small variations in state populations between the apo-receptor and the antagonist-bound receptor are below statistical significance. We discuss below the implications of these results on the basal activity, partial agonism, and inverse agonism in A_{2A} AR.

Discussion

In this study, we used smFRET to investigate the conformational dynamics of A_{2A} AR. To preserve the native conformational

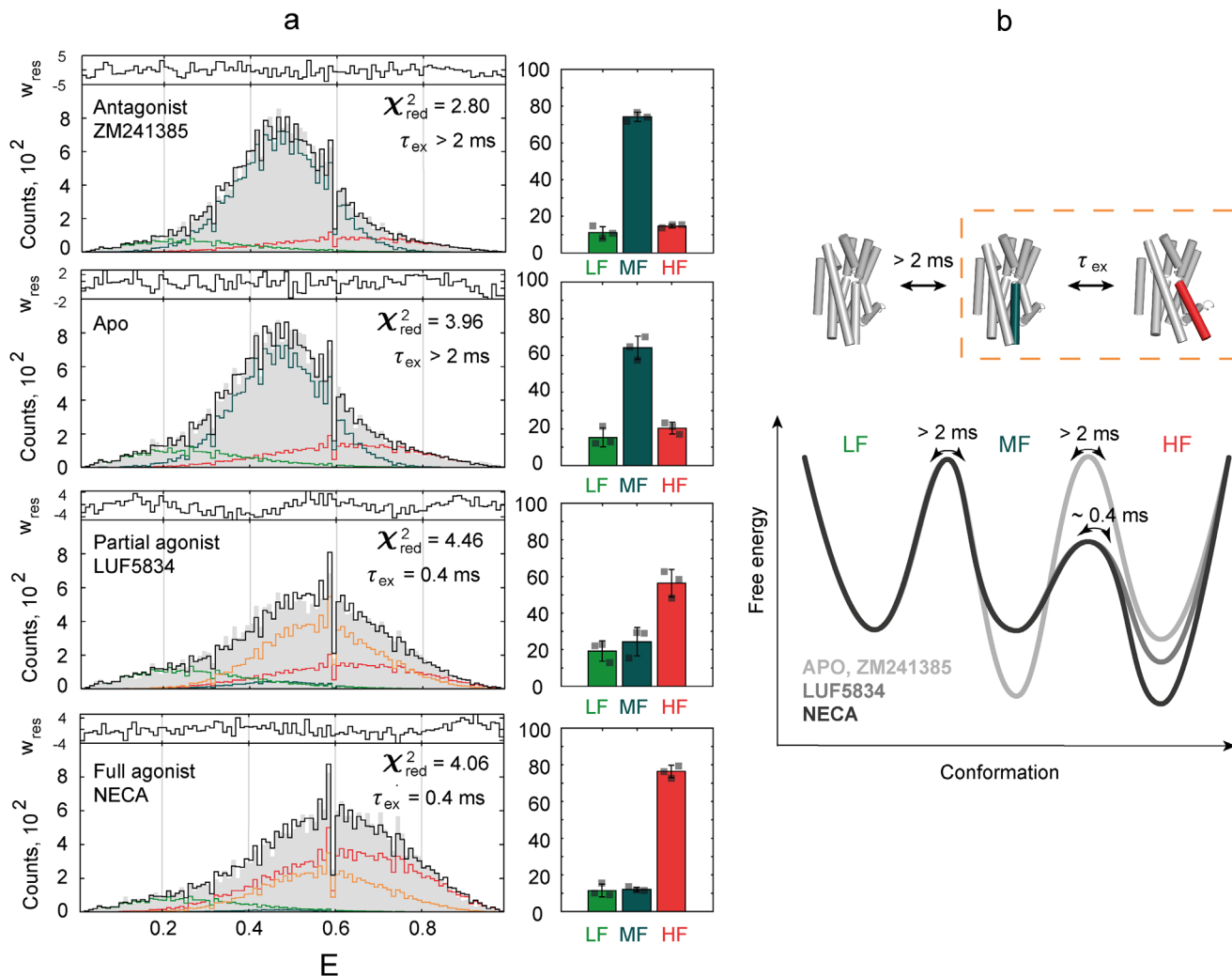


Fig. 3 PDA quantifies parameters of the $A_{2A}AR$ three-state action model by fitting FRET efficiency distributions. **a** Experimental distributions of 1-ms-long time bins derived from fluorescence bursts of double-labeled $A_{2A}AR$ (gray area) were fitted with a three-state model. The resulting fit (black line) is a sum of distributions simulated for molecules that stay in the LF (light green line), MF (dark cyan line), or HF (red line) state during the entire simulated time bin, and the distribution for molecules that sample both MF and HF states within the time bin (orange line). The fitting residuals are shown on the top of each panel. The bar charts on the right show relative populations of the three states, with error bars representing SD of $n = 3$ technical replicas with different protein aliquots. Individual data points are shown as gray squares, source data are available online as Supplementary Data 2. **b** The three-state action model of $A_{2A}AR$ and corresponding energy landscapes for the apo and agonist-bound receptor demonstrate relative populations of the states and inter-state exchange times. $\tau_{ex} = (k_{12} + k_{21})^{-1}$ is the relaxation time of the exchange between the MF and HF states (highlighted with dashed orange rectangle). TM6 is colored on the schematic (cylinder) representation of active (PDB: 5G53⁷⁰, red) and inactive (PDB: 3EML⁶⁹, dark cyan) structures of $A_{2A}AR$. The landscapes of relative energy are drawn with low FRET as a reference state.

dynamics of the receptor and minimize measurement-related artifacts we used four strategies. (1) As previous studies showed dramatic effects of commonly used detergents on GPCR conformational dynamics^{64,65}, we reconstituted the receptor in nanodiscs that provide a more relevant lipid bilayer environment. (2) To minimize the effect of fluorophores on the receptor's dynamics we used small organic dyes attached to strategically engineered cysteines. (3) We avoided the need to remove native cysteines and associated to that potential structural perturbations by using the previously developed in-membrane labeling procedure⁵². We showed that the mutant form of the receptor retains functional activity using the thermal shift assay and cAMP signaling assay in live HEK293T cells. (4) Finally, we studied receptors freely diffusing in solution and therefore excluded any artifacts related to their immobilization.

MFD-PIE fluorescence microscopy allowed us to measure and analyze FRET dynamics with a sub-millisecond temporal

resolution in the double-labeled receptor subpopulations while excluding unlabeled and single-dye labeled receptors from the analysis. Using various single-burst descriptors and time-resolved analysis methods for quantifying FRET dynamics, we revealed sub-millisecond conformational dynamics in $A_{2A}AR$. Slight deviations of bursts from the 'static FRET line' on the FRET efficiency versus donor fluorescence lifetime plot hinted at nanosecond-millisecond dynamics for the apo- $A_{2A}AR$ and $A_{2A}AR$ with each of the used ligands (Fig. 2b), although can equally be attributed to undefined systematic errors. FRET-2CDE analysis suggested more pronounced conformational dynamics in the agonist-bound $A_{2A}AR$ than in the apo or antagonist-bound $A_{2A}AR$ (Fig. 2d). BVA confirmed that the variations of FRET efficiency among $\sim 100 \mu s$ time bins exceed the level expected from shot noise (Fig. 2f). Finally, fFCS clearly confirmed the dynamics nature of the data and demonstrated two components in $A_{2A}AR$ dynamics: fast microsecond-time (3–20 μs) dynamics

present in all samples and assigned mostly to dyes photophysics and slower ($390 \pm 80 \mu\text{s}$) dynamics evoked by agonists (Fig. 2h). It is fFCS that puts all our findings in a single self-consistent picture: both fast and slow dynamics contribute to the deviation of bursts from the ‘static FRET line’, however the fast dynamics make limited contributions to the FRET-2CDE scores and to the BVA distribution deviations because of their 10-fold faster timescale compared to the temporal resolution of these techniques. Meanwhile, the slower dynamics evoked with the agonists explains the increased dynamics scores in FRET-2CDE and BVA for the agonist-bound A_{2A} AR. Finally, dynamic PDA led us to a three-state model of the A_{2A} AR conformational dynamics that could fit the measured FRET efficiency histograms consistently with the fFCS findings (Fig. 3).

While our manuscript was under review, another publication appeared, showing active and inactive states in detergent-solubilized A_{2A} AR via smFRET⁶⁶. However, no agonist-induced increase in sub-millisecond dynamics were detected, which can be related to adverse effects of detergent environment on protein dynamics.

Our final three-state model of the A_{2A} AR conformational space illustrates two effects of agonists on the A_{2A} AR: (i) the balance between MF and HF states is shifted away from the inactive-like MF towards the active-like HF, and (ii) the energy barrier between MF and HF states is lowered, as evidenced by more frequent transitions between the states (Fig. 3b). The MF and HF states are not interchangeable in the sub-millisecond time domain in the apo and antagonist-bound A_{2A} AR, but can interconvert on a 300–500 μs timescale in the agonist-bound A_{2A} AR. The least populated LF state, presumably, corresponds to receptors locked in a long-lived non-functional state or improperly folded receptors. In a good agreement with our findings, sub-millisecond agonist-induced conformational dynamics of the intracellular part of TM7¹⁷ (Y290W^{7,55}) and the N-terminal end of H8²⁰ (I292M^{8,47}) have been shown for A_{2A} AR by NMR. Although sub-millisecond dynamics between inactive-like conformations of TM6 (V229C^{6,31}) in the apo- A_{2A} AR have been reported¹⁹, our data suggest only limited dynamics in the ligand-free and antagonist-bound A_{2A} AR.

The increased sub-millisecond conformational dynamics in the agonist-bound state may have a direct relevance to protein function. One of the most prominent structural changes associated with the agonist binding to A_{2A} AR is the movement of the intracellular part of TM6 accompanied by a rotameric switch of Tyr197^{5,58} side chain (PDB ID 3QAK⁶⁷ and PDB ID 2YDV⁶⁸). In the antagonist-bound structure (PDB ID 3EML⁶⁹), Tyr197^{5,58} is placed between TM3 and TM6 forming a hydrogen bond network that tightens TM6 to the protein core. In the agonist-bound structure this residue moves outward, and the hydrogen bond network is lost. As a result, TM6 gains higher structural flexibility, an effect that we readily detected as increased sub-millisecond conformational dynamics in our experiments. In the further activation events upon G-protein binding to A_{2A} AR (PDB ID 5G53⁷⁰), the intracellular part of TM6 shifts further away from the receptor core and G-protein helix $\alpha 5$ protrudes into the created cleft. Therefore, the increased conformational dynamics may be important for the A_{2A} AR to accommodate G protein and other signaling partners.

In our experiments, we could not measure slow conformational dynamics (>2 ms), because of the short residence time of individual molecules in the microscope focal spot. Our data do not indicate long-lived states in the agonist-bound A_{2A} AR (besides the ligand-insensitive LF state), but the FRET-2CDE analysis shows only moderate dynamics scores, and the observed deviations from the ‘static FRET line’ can be explained by a microsecond plasticity within a long-lived conformation. Consequently,

we cannot exclude that long-lived conformations can coexist with conformations that show sub-millisecond dynamics. Keeping this in mind, we nevertheless did not introduce any additional long-lived states into our final model of the A_{2A} AR conformational space to avoid overfitting. Previous studies based on NMR^{19–21} and single-molecule fluorescence microscopy³² provide complementary insights into the dynamics of long-lived (>2 ms) A_{2A} AR conformations. Similarly to our study, both NMR²⁰ and single-molecule fluorescence microscopy³² detect agonist-induced increase of the receptor conformational dynamics.

The observed agonist-induced increase in FRET efficiency is unexpected based on the distances between the labeled residues (L225 and Q310) in the available crystal structures of A_{2A} AR, which suggest a decrease in the FRET efficiency, because the distance between the Ca-atoms increases from $\sim 40 \text{ \AA}$ in the antagonist-bound structure (PDB: 3EML⁶⁹) to $\sim 47 \text{ \AA}$ in the fully active structure (PDB: 5G53⁷⁰). However, since the change of the distance between labeled residues ($\sim 7 \text{ \AA}$) is smaller than the length of the flexible linkers attached to the dyes ($\sim 15 \text{ \AA}$), we hypothesize that the inverse direction of the FRET change is due to the dyes not being randomly oriented (Fig. 1b), but rather occupy preferred locations within their respective accessible volume. In line with this, constrained dynamics of the dyes were indeed observed via fluorescence depolarization measurements: within nanoseconds after fluorescence excitation, anisotropy reached stable values (r_p) of 0.12–0.16 for the donor and 0.22–0.23 for the acceptor (Supplementary Fig. 13, Supplementary Table 7, “Fluorescence depolarization measurements” in “Methods”). These stable values correspond to wobbling within a cone with semi-angle of 43–49° or 34–35°, respectively, and are almost unaffected by ligands. To get further insights into the preferred locations of the dyes we performed 1- μs -long molecular dynamics (MD) simulations, which revealed that the dye attached to TM6 might indeed preferentially locate between the intracellular tips of TM3 and TM5 in the inactive conformation and enter the G-protein-binding cavity of the receptor in the fully active conformation (Supplementary Figs. 14–16, “Molecular dynamics simulations” in “Methods”). These preferred conformations of the dye would result in a significant decrease of the mean inter-dye distance upon receptor activation (from 5 nm to 3 nm, Supplementary Fig. 15), which would in turn lead to an increase in the mean FRET efficiency. Thus, our MD simulations provide a plausible explanation for the observed increase in the FRET efficiency upon A_{2A} AR activation and show that the observed FRET changes agree with the available crystal structures of A_{2A} AR.

The PDA analysis of our data suggests that the partial agonist LUF5834 and the full agonist NECA stabilize $56 \pm 8 \%$ and $76 \pm 3 \%$ of A_{2A} ARs, respectively, in the same active-like HF conformation (mean \pm SD, three technical replicas with different protein aliquots). A similar mechanism for partial agonism in A_{2A} AR has recently been demonstrated by NMR with isotope-labeled methionine residues located in different structural domains (I106M^{3,54}, M140^{4,61}, M211^{5,72}, and I292M^{8,47}) of the receptor²⁰. On the other hand, other NMR-based studies have suggested that LUF5834 either stabilizes a distinct, not a fully active conformation^{19,24}, or has no effect on the A_{2A} AR conformation²¹. Our data do not support the existence of a separate partially active conformation of A_{2A} AR stabilized with LUF5834 that would be distinct from the fully active conformation stabilized with NECA. On the other hand, we cannot exclude that such partially active state could not be resolved in our data because small differences in FRET efficiency, the high photon shot noise in single-molecule experiments, or the broadening of the FRET-distribution due to variations of photophysical parameters of the dyes.

In addition, we observed that $20 \pm 3\%$ of apo $A_{2A}ARs$ exhibit an active-like HF state (Fig. 3a). It may be a reason for a moderate basal activity of the receptor, however the role the intracellular signaling partners cannot be excluded. Two previous NMR-based studies have addressed the molecular mechanisms of $A_{2A}AR$ basal activity. One study reported a 70% population of pre-active and fully active states in the apo-ensemble¹⁹. Another study has reported negligible basal activity and showed that in the agonist-bound $A_{2A}AR$ unique previously unpopulated conformations emerge²¹. A recent review suggests that discrepancies between these two works could arise from differences in used constructs, ¹⁹F reporters, their attachment sites, or in selected membrane-mimicking systems (MNG/CHS versus DDM/CHS micelles)⁷¹. A recent NMR-based study with $A_{2A}ARs$ in nanodiscs reported a 50% population of active states in the apo-ensemble²³. The contradictory estimations of the basal activity of $A_{2A}AR$ should be put in the context of a similar heterogeneity of results provided by cell-based signaling assays. In different experiments, the basal activity of $A_{2A}AR$ was reported to reach from 0 to 20%^{69,72–74}, to 20–40%^{46,75,76}, or even 40–70%^{77–80}. Cell assays are affected by different $A_{2A}AR$ expression levels and cell lines used^{73,79}. It has been shown that the C-terminal truncation of $A_{2A}AR$ impairs its basal activity—this can play an important role for our study as well as previous NMR-based works⁷⁵.

Finally, our measurements show that ZM241385 does not change the distribution of FRET efficiency compared to apo conditions and therefore we do not observe inverse agonism of ZM241385. Because many studies reported negligible basal activity of $A_{2A}AR$, ZM241385 is widely referred to as $A_{2A}AR$ antagonist^{11,69,81}. The recent ¹⁹F-NMR study, where no basal activity was detected for $A_{2A}AR$, correspondingly did not register any conformational changes induced with ZM241385²¹. On the other hand, those works that identified significant basal activity of $A_{2A}AR$ frequently reported inverse agonism of ZM241385^{46,73,74,76,79,82}. In line with these findings, the ¹⁹F-NMR study that has reported 70% basal activity also showed inverse agonism of ZM241385¹⁹. Notably, it was previously shown that ZM241385 can lose inverse agonist activity if tested not in cells, but in isolated membranes⁷⁵. This latter result suggests that intracellular interaction partners can play an important role in both basal activity and inverse agonism, explaining both heterogeneity in published functional data and our results.

The multi-state conformational behavior of GPCRs delineates their complex pharmacology and, therefore, challenges modern drug design. We believe that new methods showing how GPCR activity is modulated on a molecular level will facilitate the design and discovery of drugs with novel beneficial properties. Here we demonstrated a strategy to observe conformational dynamics of a GPCR in solution, yet in a close-to-physiological environment of lipid nanodiscs using intramolecular smFRET measured via the MFD-PIE approach. Our measurements combined fluorescence intensity, lifetime, and anisotropy information to characterize the sub-millisecond conformational dynamics of TM6 and H8 in $A_{2A}AR$ and shed light on molecular mechanisms of basal activity and partial agonism in the receptor. The general strategy developed in our work can be extended to study the effects of various modulators (ligands, ions, lipids, etc.), membrane-mimicking systems (micelles, lipid nanodiscs, liposomes, etc.) and genetic modifications on the activity of $A_{2A}AR$ and, in perspective, other GPCRs.

Limitations of the study. In this study, we used smFRET to investigate the dynamics of the $A_{2A}AR$. The intrinsic limitation of FRET as a label-based method is that the dynamics of dyes and protein cannot be completely separated based on fluorescence

data. Our nanosecond-time fluorescence depolarization measurements (Supplementary Fig. 13 and Supplementary Table 7) and microsecond-long MD simulations (Supplementary Figs. 14 and 15) indicate that the reorientation of the dyes attached to $A_{2A}AR$ upon conformational change of the protein strongly affects the measured FRET efficiency. This means that changes in FRET efficiency should not be interpreted exclusively as distance changes, and, particularly, apparent distances measured in PDA should only be considered as parameters of the fit, not as physical distances between the dyes. In addition, we cannot completely exclude that the dynamics of the dyes contribute to the observed 390- μ s dynamics. However, fluorescence depolarization measurements suggest that the orientational freedom of the dyes is almost ligand independent (Supplementary Fig. 13 and Supplementary Table 7) and burst-wise anisotropy measurements do not indicate multiple long-lived states of the dyes on the millisecond timescale (Supplementary Fig. 17, “Burst-wise steady-state fluorescence anisotropies” in “Methods”). Therefore, we assign the agonist-induced dynamics observed in our data to the dynamics of the receptor. This interpretation is supported by previous NMR-based studies that also observed agonist-induced dynamics in $A_{2A}AR$ on a sub-millisecond timescale^{17,20}.

Methods

Protein expression, purification and labeling. The gene encoding the human $A_{2A}AR$ (UniProt C9JQD8) C-terminally truncated after residue Ala 316 (Supplementary Fig. 1a) was synthesized de novo (Eurofins). The nucleotide sequence was optimized for *Leishmania tarentolae* expression with the GeneOptimizer software (ThermoFisher Scientific). KpnI restriction site was introduced at the C-terminus and used for polyhistidine tag (H9) fusion. The final construct was cloned into the integrative inducible expression vector pLEXSY_I-blecherry3 (Jena Bioscience, Germany) via the BglII and NotI restriction sites. L225C^{6,27} and Q310C^{8,65} mutations were introduced by PCR.

Leishmania tarentolae cells of the strain LEXSY host T7-TR (Jena Bioscience) were transformed with the $A_{2A}AR$ expression plasmids linearized by the SmaI restriction enzyme. After clonal selection, the transformed cells were grown at 26 °C in the dark in shaking baffled flasks in Brain-Heart-Infusion Broth (Carl Roth, Germany) supplemented with 5 μ g/mL Hemin (AppliChem), 50 U/mL penicillin and 50 μ g/mL streptomycin (both antibiotics from AppliChem). When $OD_{600} = 1$ was reached, 10 μ g/mL tetracycline was added, and incubation continued for an additional 24 h.

The harvested cells were disrupted in an M-110P Lab Homogenizer (Microfluidics) at 10,000 psi in a buffer containing 50 mM NaH_2PO_4/Na_2HPO_4 , pH 7.6, 0.2 M NaCl, 20 mM KCl, 10 mM $MgCl_2$, 10% glycerol (w/v), 1 mM EDTA, 2 mM 6-aminohexanoic acid (AppliChem), 50 mg/L DNase I (Sigma-Aldrich) and cOmplete protease inhibitor cocktail (Roche). The membrane fraction of the cell lysate was isolated by ultracentrifugation at 120,000 $\times g$ for 1 h at 4 °C. The pellet was resuspended in the same buffer but without DNase I and stirred for 1 h at 4 °C. The ultracentrifugation step was repeated again.

Finally, the membranes were resuspended in the labeling buffer containing 50 mM HEPES, pH 7.0, 10 mM $MgCl_2$, 20 mM KCl, 2 mM 6-aminohexanoic acid, and cOmplete and mixed with Atto643-maleimide (ATTO-TEC) and Alexa488 maleimide (Invitrogen), dissolved in dimethyl sulfoxide (0.5 mg of each fluorescent label per 10 g of cells). Labeling reactions were carried out overnight in the dark at 4 °C on a roller mixer.

The next day, membrane fractions were pelleted by ultracentrifugation at 120,000 $\times g$ for 1 h at 4 °C and washed twice with the labeling buffer for removal of unbound fluorescent labels. For solubilization, membranes were resuspended in a buffer containing 20 mM HEPES, pH 8.0, 800 mM NaCl, 5 mM $MgCl_2$, 10 mM KCl, 2 mM 6-aminohexanoic acid, cOmplete with 4 mM theophylline (Sigma-Aldrich) and 1% n-Dodecyl β -maltoside (DDM) (Glyco Biochemicals)/0.2% cholesteryl hemisuccinate (CHS) (Merck) (w/v) and left on the stirrer for 2 h at 4 °C in the dark. The insoluble fractions were removed by ultracentrifugation at 120,000 $\times g$ for 1 h at 4 °C. The supernatants were loaded on an Ni-NTA resin (Cube Biotech) and incubated in the batch mode overnight in the dark at 4 °C.

The next morning, proteins bound to Ni-NTA resin were washed with 10-column volumes of the first washing buffer: 50 mM HEPES, pH 7.5, 800 mM NaCl, 25 mM imidazole, 10 mM $MgCl_2$, 8 mM ATP (Sigma-Aldrich), 2 mM 6-aminohexanoic acid, 0.1 mM phenylmethylsulfonyl fluoride, 4 mM theophylline, cOmplete, 0.1% DDM / 0.02% CHS. Then, columns were washed with 10-column volumes of the second washing buffer: 50 mM HEPES, pH 7.5, 800 mM NaCl, 50 mM imidazole, 2 mM 6-aminohexanoic acid, 0.1 mM phenylmethylsulfonyl fluoride, 4 mM theophylline, cOmplete, 0.1% DDM/0.02% CHS (w/v). Finally, proteins were eluted with 5-column volumes of the elution buffer: 25 mM HEPES, pH 7.5, 800 mM NaCl, 220 mM imidazole, 2 mM 6-aminohexanoic acid, 0.1 mM

phenylmethylsulfonyl fluoride, cOmplete, 0.1% DDM/0.02% CHS (w/v). The eluates were subjected to size-exclusion chromatography on a Superdex 200 Increase 10/300 GL column (GE Healthcare Life Sciences) in a buffer containing 20 mM HEPES, pH 7.5, 800 mM NaCl, 1 mM EDTA, 2 mM 6-aminohexanoic acid, cOmplete, 0.05% DDM/0.01% CHS (w/v). Fractions, corresponding to $A_{2A}AR$ monomers, were pulled and subjected to nanodisc reconstitution.

Nanodisc reconstitution. Membrane Scaffold Protein 1D1 (MSP1D1) was expressed in *E. coli* using gene with an N-terminal 6XHis-tag and upstream TEV-protease site cloned into pET28a(+) (Addgene plasmid #20061⁵³). MSP1D1 was purified using IMAC⁸³ with further cleavage of 6xHis-tag by TEV protease (Sigma-Aldrich). The lipid mixture of 1-palmitoyl-2-oleoyl-sn-glycero-3-phosphocholine (POPC): 1-palmitoyl-2-oleoyl-sn-glycero-3-phospho-(1'-rac-glycerol) (POPG) (Avanti Polar Lipids) in chloroform was prepared at a molar ratio 7:3. The lipid film was dried under a gentle nitrogen stream, followed by removal of the solvent traces under vacuum, and then solubilized in 200 mM sodium cholate. The purified $A_{2A}AR$ in DDM/CHS micelles was mixed with MSP1D1 and the POPC:POPG lipids at a molar ratio $A_{2A}AR:MSP1D1:lipids = 0.2:1:60$. The final sodium cholate concentration was adjusted to 20 mM, the typical final receptor concentration was 0.1 mg/mL. After 1 h of incubation at 4 °C, the mixture was incubated with wet Bio-Beads SM-2 (Bio-Rad, 0.4 g of beads for 1 mL reaction, beads were washed in methanol and equilibrated with 20 mM HEPES, pH 7.5, 800 mM NaCl, 1 mM EDTA) overnight at 4 °C in the dark. The next morning, the beads were discarded and the supernatant was supplemented with a fresh portion of Bio-Beads for an additional 4 h incubation. Finally, $A_{2A}AR$ reconstituted into nanodiscs was subjected to size-exclusion chromatography on a Superdex 200 Increase 10/300 GL column (GE Healthcare) in a buffer containing 20 mM HEPES, pH 7.5, 150 mM NaCl, 1 mM EDTA, 2 mM 6-aminohexanoic acid, cOmplete. Labeling efficiencies of 26% (Alexa488) and 8% (Atto643) were obtained for the mutant $A_{2A}AR$ (Supplementary Table 1). The low labeling efficiency is, probably, a consequence of labeling the receptors directly in isolated membrane pellets, a strategy we adopt to avoid mutating out native cysteines protected by the native lipid bilayer from labeling. Fractions containing labeled receptors were combined together and used for further experiments.

Fluorescence spectra characterization. For fluorescence spectra characterization, diluted (<5 μM) apo- $A_{2A}AR$ samples were placed in a quartz cuvette (10 mm path length). Excitation and emission spectra were recorded using an Edinburgh Instruments FLS980 spectrometer corrected for the wavelength-dependent throughput and sensitivity of the detector. Fluorescence in the acceptor's emission spectral range after irradiation in the donor's excitation spectral range indicated FRET in the double-labeled receptor samples (Supplementary Fig. 1c).

Ensemble-based fluorescence lifetime measurements. The time-resolved detection of the fluorescence decay of Apo- $A_{2A}AR$ labeled with Alexa488 and Atto643 was performed with a Fluotime100 fluorescence spectrophotometer (Picoquant, Berlin, Germany) based on a picoHarp300 unit and using a pulsed diode laser (LDH-440; center wavelength 440 nm; pulse width 54 ps; repetition frequency 10 MHz) as an excitation source. Fluorescence decay curves were measured at 665 nm under magic angle conditions by time-correlated single-photon counting (TCSPC) allowing to determine fluorescence lifetimes down to 100 ps⁸⁴. Decay curves were analyzed by iterative reconvolution of the instrument response function, IRF(t), with an exponential model function, M(t), using the FluoFit software (version 4.4; Picoquant).

Fitting the measured TCSPC-delay signal with a monoexponential decay (Supplementary Fig. 1d) did not allow a satisfactory description of the acceptor fluorescence intensity time trace, while a biexponential fit was sufficient and yielded two components: one with a positive amplitude (normal fluorescence decay) and one with a negative amplitude (rise term). The rising term is expected for FRET and cannot originate exclusively from the direct excitation of Atto643 with a 440-nm laser. Therefore, fluorescence lifetime measurements of labeled mutant protein in bulk solution also confirmed that there is a fraction of double-labeled receptors that exhibit FRET in the sample.

Thermal shift assay. To show that the $A_{2A}AR$ mutant (L225C^{6.27}/Q310C^{8.65}) retains ligand-binding activity in lipid nanodiscs, we used the fluorescent thermal stability assay⁵⁴. The studies were carried out on a Rotor-Gene Q 6 plex (QIAGEN) instrument at a heating rate of 2 °C/min and a temperature range of 25–90 °C. The excitation wavelength was set at 387 nm and the emission wavelength was 463 nm. The $A_{2A}AR$ concentration was about 2 μM . Buffer conditions: 20 mM HEPES, 150 mM NaCl, 1 mM EDTA, 2 mM 6-aminohexanoic acid, pH 7.5. To obtain a good fluorescence intensity we used a 2.5-fold molar excess of CPM dye (7-Diethylamino-3-(4'-Methylimidazolylphenyl)-4-Methylcoumarin, Invitrogen) to protein. To prepare protein for the ligand-binding measurements, we added 200 μM of ZM241385 or NECA and incubated for 1 h in the dark at 4 °C. The thermal denaturation assay was performed in a total volume of 50 μL (Supplementary Fig. 1e).

Measurement of $A_{2A}AR$ surface expression and Gs-signaling. For $A_{2A}AR$ functional assays, the $A_{2A}AR$ (WT or L225C^{6.27}/Q310C^{8.65} mutant, both

C-terminally truncated after residue Ala 316) gene (GenScript) was optimized for eukaryotic expression with an N-terminal hemagglutinin signal sequence (MKTIIALSYIFCLVFA) followed by the FLAG tag epitope (DYKDDDDK) and C-terminal 10xHis tag were cloned into pcDNA3.1(-) at BamHI(5') and HindIII(3'). The surface expression of $A_{2A}AR$ was determined by the whole-cell ELISA assay⁸⁵. Briefly, HEK293FT cells were seeded in a 100 mm cell culture plate and transfected separately with 10 μg of each expression plasmid DNA (pcDNA3.1(-) $A_{2A}AR$ (WT), pcDNA3.1(-) $A_{2A}AR$ (L225C^{6.27}/Q310C^{8.65}) or pcDNA3.1(-) as a negative control) using a common Lipofectamine 3000 protocol. The plates were incubated for an additional 12–18 h at 37 °C, 5% CO₂. The HRP-conjugated anti-FLAG M2 antibody (A8592, Sigma) at a dilution of 1:2000 in TBS with 1% protease-free BSA (A3059, Sigma) and TMB ready-to-use substrate (T0565, Sigma) were used for the ELISA procedure. For normalization on cells quantity Janus Green B (Sigma) staining was used, and the absorbance ratio A_{450}/A_{595} was calculated. Measurements were performed in triplicate for WT and mutant $A_{2A}AR$ as well as for empty-vector-transfected cells. Measured values of A_{450}/A_{595} were normalized so that the mean expression level of WT $A_{2A}AR$ was 100% ($F_{WT} = 100 \pm 6\%$, SDs for $n = 3$ measurements are given). The double-mutant form of the receptor showed only slightly lower expression level than WT: $F_{L225C/Q310C} = 73 \pm 7\%$. Empty-vector-transfected cells showed only marginal anti-FLAG antibody binding: $F_{EV} = 1 \pm 1\%$.

For evaluation of the $A_{2A}AR$ signaling activity, we checked the effect of the agonist NECA on cAMP responses in transfected cells. For cAMP determination, we used the Bioluminescence Resonance Energy Transfer (BRET) approach with the EPAC biosensor⁸⁶. The cAMP BRET biosensor was kindly provided by professor Raul Gainetdinov⁸⁷. Transfections were carried out with Lipofectamine 3000 (Thermo) using HEK293T cells seeded in a 100 mm cell culture plate, receptor cDNA vectors pcDNA3.1(-) $A_{2A}AR$ (WT, residues 1–316), pcDNA3.1(-) $A_{2A}AR$ (Q310C^{8.65}/L225C^{6.27}, residues 1–316) or empty pcDNA3.1(-) vector (10 μg each) and the EPAC biosensor cDNA vector (1 μg) needed for evaluation of the cAMP production. Transfected cells were split into 96-well plates at 10⁵ cells per well. On the following day, 70 μL of PBS were added to each well followed by the addition of 10 μL of a 50 μM coelenterazine-h solution (Promega). After 10-min incubation, either 10 μL of buffer or 10 μL of NECA at different concentrations in PBS were added, and the plate was then placed into a CLARIOstar reader (BMG LABTECH, Germany) with a special BRET filter pair (475 \pm 30 nm—coelenterazine-h and 530 \pm 30 nm—YFP). The BRET signal was calculated as the ratio of the light emitted at 530 nm to the light emitted at 480 nm. Three independent experiments with three technical replicas in each were conducted. For pEC₅₀ evaluation, dose-response curves from three technical replicas were averaged and analyzed. Mean and SD of pEC₅₀ among three biological samples were calculated (Supplementary Fig. 1f). A lack of agonist-induced BRET changes in cells transfected with an empty vector confirmed that signaling from the endogenous $A_{2A}AR$ in HEK293T cells is negligible.

Confocal MFD-PIE setup. For single-molecule experiments, a home-built multi-parameter fluorescence detection microscope with pulsed-interleaved excitation (MFD-PIE)³⁹ was used (see scheme of the setup in Supplementary Fig. 2). Two lasers were used: a pulsed 483-nm laser diode (LDH-P-C-470, Picoquant) and a pulsed 635-nm laser diode (LDH-P-C-635B, Picoquant), with alternating at 26.67 MHz pulses, delayed by 18 ns with respect to each other. Sample emission was transmitted through a pinhole and spectrally split. Both, the blue range and red range were split by polarization into two detection channels. Photons were detected by four avalanche photodiodes (PerkinElmer or EG&G SPCM-AQR12/14, or Laser Components COUNT BLUE): B_{||} (blue-parallel), B_⊥ (blue-perpendicular), R_{||} (red-parallel) and R_⊥ (red-perpendicular) (Supplementary Fig. 2), which were connected to a TCSPC device (SPC-630, Becker & Hickl GmbH). Microscope alignment (excitation light guiding, objective lens correction collar, pinhole, detectors) was done using real-time fluorescence correlation spectroscopy (FCS) on freely diffusing Atto488-COOH and Atto655-COOH in water. For more details about the used equipment the reader is referred to ref. ⁸⁸.

smFRET data recording. Samples of double-labeled $A_{2A}AR$ in nanodiscs were diluted in a buffer, containing 20 mM HEPES, pH 7.5, 150 mM NaCl, 1 mM EDTA, 2 mM 6-aminohexanoic acid to a protein concentration of 0.5–2 nM. To measure the effects of ligand binding, samples were supplemented with either 10 μM ZM241385, 10 μM LUF5834 or 10 μM NECA and incubated for 30 min at 4 °C. After the incubation, the samples were transferred to a Nunc Lab-Tek Chambered coverglass (Thermo). smFRET experiments were performed at 100 μW of 483 nm and 50 μW of 635 nm excitation. Measurements were recorded at room temperature (22 °C), samples were replenished every 30 min. With all filters applied (see Selection of double-labeled, donor-only and acceptor-only subpopulations), 9000–12,000 bursts corresponding to double-labeled molecules were collected for each sample: 11,961 for apo, 10,167 burst for ZM241385, 9557 for LUF5834, and 11,007 for NECA. Background scattering information was obtained via a buffer measurement under identical conditions.

Burst identification. For single-molecule data, we employed a two-color MFD all-photon burst search algorithm⁶³ using a 500- μs sliding time window (min. 50

photons per burst, min. five photons per time window). A 0–20-ms burst duration cutoff was applied to remove sparse (<1%) slow-moving aggregates.

Selection of double-labeled, donor-only, and acceptor-only subpopulations.

To select single-labeled or double-labeled subpopulations of molecules, we used specific restrictions for the stoichiometry S , FRET efficiency E , fluorescence lifetime, anisotropy, and kernel-density estimator ALEX-2CDE, as shown below.

Donor-only molecules: $ALEX-2CDE > 20$, $-0.1 < E < 0.1$, $0.9 < S < 1.1$, $0.1 \text{ ns} < \tau_D < 6 \text{ ns}$, $-0.2 < r_D < 0.6$.

Acceptor-only molecules: $ALEX-2CDE > 20$, $0.6 < E < 1.1$, $-0.1 < S < 0.2$, $0.1 \text{ ns} < \tau_A < 8 \text{ ns}$, $-0.2 < r_A < 0.6$.

Double-labeled molecules: $ALEX-2CDE < 15$, $0.1 < E < 1.0$, $0.2 < S < 0.8$, $0.1 \text{ ns} < \tau_D < 4.5 \text{ ns}$, $0.1 \text{ ns} < \tau_A < 8 \text{ ns}$, $-0.2 < r_D < 0.6$, $-0.2 < r_A < 0.6$.

FRET efficiency and stoichiometry. The absolute burst-averaged FRET efficiency E was calculated as:

$$E = \frac{F_{BR} - ct \cdot F_{BB} - de \cdot F_{RR}}{\gamma F_{BB} + F_{BR} - ct \cdot F_{BB} - de \cdot F_{RR}} \quad (1)$$

where $F_{BR} = S_{BR} - B_{BR}$ is the background-corrected number of photons in the red detection channels independently of the polarization after blue excitation (with S_{BR} and B_{BR} being the summed intensity and background, respectively, in the time gates BR_{\parallel} and BR_{\perp}); $F_{BB} = S_{BB} - B_{BB}$ is the background-corrected number of photons in the blue detection channels after blue excitation (with S_{BB} and B_{BB} being the summed intensity and background, respectively, in the time gates BB_{\parallel} and BB_{\perp}), $F_{RR} = S_{RR} - B_{RR}$ is the background-corrected number of photons in the red detection channels after red excitation (with S_{RR} and B_{RR} being the summed intensity and background, respectively, in the time gates RR_{\parallel} and RR_{\perp}), de —the correction factor for direct excitation of the acceptor with the 483 nm laser, ct —the correction factor for the emission crosstalk of the donor in the acceptor channel, and γ —the relative detection efficiency of the donor and acceptor³⁹.

The corrected stoichiometry ratio S was calculated with:

$$S = \frac{\gamma F_{BB} + F_{BR} - ct \cdot F_{BB} - de \cdot F_{RR}}{\gamma F_{BB} + F_{BR} - ct \cdot F_{BB} - de \cdot F_{RR} + \beta F_{RR}} \quad (2)$$

where β -factor accounts for different detection efficiencies of the donor and the acceptor.

Correction factors. For correction, first, the background was subtracted from the experimental signals. Then, the donor emission crosstalk ($ct = 0.0059$) and acceptor direct excitation ($de = 0.024$) factors were determined directly from the measurements and applied to correct the data³⁹. For correction purposes, we preliminarily (see the final selection criteria for other analyses in the section “Selection of double-labeled, donor-only and acceptor-only subpopulations”) selected double-labeled molecules using the kernel-density estimator (ALEX-2CDE < 15)⁴², FRET efficiency ($0.1 < E < 1$), and stoichiometry ($0.2 < S < 0.6$), corrected for channel crosstalk (ct) and direct excitation (de). For these selected molecules, E was plotted vs $1/S$, and a straight line was fitted to obtain the correction factors:

$$\gamma = \frac{\Omega - 1}{\Omega + \Sigma - 1} \quad (3)$$

$$\beta = \Omega + \Sigma - 1, \quad (4)$$

where Ω is the intercept and Σ is the slope of the fit. Finally, $\gamma = 0.69$ and $\beta = 1.9$ were obtained.

Burst-wise fluorescence lifetime. To estimate the single-molecule burst-averaged fluorescence lifetimes of the donor (τ_D) and acceptor (τ_A), the maximum likelihood estimator approach was used⁸⁹.

To test whether the deviations of bursts from the static FRET line are statistically significant, experimental measurements were supplemented with simulations. Experimental bursts were grouped in $N = 50$ intervals equally spaced by the burst-wise FRET efficiency. Groups with less than 200 bursts were excluded from the analysis.

Then, for each burst a distance $R_i(E_i)$ was determined so that a simulated normal distance distribution with the linker-related standard deviation $\sigma = 6 \text{ \AA}$ centered around R_i provided a mean FRET efficiency E_i given the Förster distance $R_0 = 49 \text{ \AA}$.

Within a burst, for each photon in the donor channel, one distance R_{ij} was simulated from the normal distribution with a mean distance R_i and a standard deviation σ . For each generated distance, corresponding theoretical FRET efficiency ($E_{ij}(R_{ij})$) and fluorescence lifetime ($\tau_{ij}(R_{ij})$) were calculated. Also, for each photon, a simulated photon arrival time (t_{ij}) was generated as a random variable with exponential distribution given the theoretical fluorescence lifetime ($\tau_{ij}(R_{ij})$).

The intensity-weighted fluorescence lifetime (τ_{INT}) was calculated across all photons belonging to all bursts within a group with $(1-E_{ij})$ weights:

$$\tau_{INT} = \frac{\sum_{ij} t_{ij}(1 - E_{ij})}{\sum_{ij} (1 - E_{ij})} \quad (5)$$

The simulation was repeated 100 times. The confidence interval for the intensity-weighted donor lifetime was calculated using the standard deviation across the simulated values, significance level $\alpha = 0.001$, and Bonferroni correction for multiple groups. Finally, we compared the experimental intensity-weighted donor lifetime τ_{INT} with the upper border of the confidence interval (Supplementary Fig. 4).

This approach was established in the PAM software and the code is available online⁹⁰.

FRET-2CDE analysis. The FRET-2CDE scores for individual bursts were calculated with the time-kernel 100 μs as described previously⁴².

To test whether the deviations of bursts from the static FRET-2CDE line were statistically significant, experimental bursts were grouped in $N = 50$ intervals equally spaced in the burst-wise FRET efficiency. Groups with less than 200 bursts were excluded from the analysis.

Then we run a simulation, in which photons in each burst were randomly “re-colored” with donor and acceptor channel probabilities corresponding to the burst-wise FRET efficiency. Weighted FRET-2CDE values were calculated for each group:

$$FRET - 2CDE = 110 - 100 \cdot \left(\frac{\sum N_D E_D}{\sum N_D} + \frac{\sum N_A (1 - E_A)}{\sum N_A} \right), \quad (6)$$

where N_D and N_A are numbers of donor and acceptor photons per burst, and E_D and $(1-E)_A$ were calculated for each burst as described in ref. ⁴².

The simulation was performed 1000 times. The mean weighted FRET-2CDE and the 99.9% confidence intervals (with Bonferroni correction) were calculated for each group. Weighted FRET-2CDE values observed in $A_{2A}AR$ data exceed the calculated confidence intervals (Supplementary Fig. 5).

Burst variance analysis (BVA). BVA was performed as described⁴³. Each fluorescence burst was segmented into M_i bins of $n = 5$ consecutive photons; the proximity ratio ϵ_{ij} was calculated for each bin by the ratio N_a/n , where N_a is the number of acceptor photons within the bin. The burst-wise proximity ratio PR_i was calculated for each burst by the ratio N_a/N , where N is the total number of photons within the burst and N_a is the number of acceptor photons within the burst. From the resulting set $\{\epsilon_{ij}\}$ and the burst-wise proximity ratio PR_i , the standard deviation is estimated as:

$$s_i = \sqrt{\frac{1}{M_i} \sum_{j=1}^{M_i} (\epsilon_{ij} - PR_i)^2}. \quad (7)$$

The burst-wise s_i values were plotted against burst-wise FRET efficiency.

Bursts were grouped in $N = 20$ equally spaced intervals by the burst-wise proximity ratio PR_i only groups with >100 bursts were analyzed. Within each group, the mean value of $\{\epsilon_{ij}\}$ was determined, and the corresponding FRET efficiency value was calculated using correction factors ct , de , γ , and β (eq. 29 from ref. ⁹¹):

$$E = \frac{1 - (1 + ct + \gamma\beta \cdot de)(1 - PR)}{1 - (1 + ct - \gamma)(1 - PR)} \quad (8)$$

The standard deviation of $\{\epsilon_{ij}\}$ within each group was plotted against FRET efficiency.

For comparison, the theoretical ‘static’ standard deviation s was determined:

$$s = \sqrt{\frac{PR(1 - PR)}{n}}. \quad (9)$$

The 99.9% confidence interval for s was determined from simulated “static” bursts, given the same number of bursts in each group. The theoretical “static” standard deviation and confidence intervals were plotted against corrected FRET efficiency (Fig. 2d).

Filtered fluorescence correlation spectroscopy (fFCS). The mathematical background of fFCS was described in detail⁹². We built two reference TCSPC patterns corresponding to the “low-FRET” pseudo-species (p_j^{LF}) and “high-FRET” pseudo-species (p_j^{HF}) (Supplementary Fig. 7). For this, we merged all four smFRET datasets with different ligand conditions; bursts corresponding to double-labeled receptors with $E < 0.3$ were used to build p_j^{LF} , bursts corresponding to double-labeled receptors with $E > 0.7$ were used to build p_j^{HF} . TCSPC channels for $BB_{\parallel}, BB_{\perp}, BR_{\parallel},$ and BR_{\perp} excitation and emission channels were stacked into a single array and indexed with j for global analysis. Using the reference TCSPC patterns, p_j^{LF} and p_j^{HF} filters f_j^{LF} and f_j^{HF} were calculated as described⁹². To reduce noise in fFCS filters, at this step TCSPC bin was increased to 100 μs .

Using the reference filters f_j^{LF} and f_j^{HF} and the fluorescence signal S_p , the correlation function $G(\tau)$ was calculated for each dataset:

$$G(\tau)^{(i,m)} = \frac{\langle (\sum_{j=1}^C f_j^{(i)} S_j(\tau)) \cdot (\sum_{j=1}^C f_j^{(m)} S_j(\tau)) \rangle}{\langle (\sum_{j=1}^C f_j^{(i)} S_j(\tau)) \rangle \cdot \langle (\sum_{j=1}^C f_j^{(m)} S_j(\tau)) \rangle} - 1. \quad (10)$$

Only bursts from double-labeled molecules were taken into account; a 10 ms time window was introduced to reduce artifacts related to the sub-ensemble FCS analysis.

The cross-correlation function $G^{LF,HF}$ was fit using equation:

$$G^{(LF,HF)}(\tau) = G_{diff}(\tau) \left(1 - A_1 e^{-\frac{\tau}{\tau_1}} - A_2 e^{-\frac{\tau}{\tau_2}} \right) + y_0, \quad (11)$$

where the diffusion-limited term is:

$$G_{diff}(\tau) = \frac{1}{\sqrt{8N}} \frac{1}{(1 + \tau/\tau_{diff})(1 + \tau/p^2\tau_{diff})^{1/2}}, \quad (12)$$

The resulting cross-correlation curves were normalized using N and offset y_0 and plotted in Fig. 2h. The 95% confidence intervals for the fitting parameters were calculated using the numerical Jacobian matrix.

Photon distribution analysis (PDA). Dynamic PDA was carried out to quantify the populations of FRET states and account for the conformational dynamics revealed by other analysis approaches^{62,93}. Practically, for each smFRET dataset, raw bursts were re-binned in different time bins (0.5, 1, and 2 ms), and three histograms were constructed and analyzed simultaneously. Only bins with at least 20 and maximally 300 photons (to reduce calculation time) were further analyzed using PDA. Bins with uncorrected stoichiometry S_{PR} below 0.2 or above 0.6 were removed from the analysis, because of suspected complex acceptor photophysics or photobleaching. Correction parameters $\gamma = 0.69$, $ct = 0.0059$ and $de = 0.024$, as well as the average background count rates in the donor and the acceptor channels after donor excitation were used to calculate the corrected FRET efficiency for PDA. The mean and width of all Gaussian distributed sub-states were globally optimized over all (three ligand and apo) conditions. State areas A_i for static states and interconversion rates constants k_{12} and k_{21} for dynamic states were optimized for each sample. An fFCS-constrained PDA fit was performed with a fixed exchange time $\tau_{ex} = (k_{12} + k_{21})^{-1}$ and k_{12}/k_{21} ratio optimized globally for each sample. The exchange time was fixed to values determined from fFCS ($\tau_{ex} = \tau_2$) for agonists, and to virtual infinity (>100 ms) for the antagonist-bound or apo receptors (to account for reduced amplitude of dynamic term). Experimental corrected FRET efficiency histograms were fitted using a reduced χ^2 -guided simplex search algorithm. The resulting parameters are presented as the means \pm SD of three technical replicas with different protein aliquots in Supplementary Fig. 12 and Supplementary Table 6). For the two-state PDA, the population of the static state A_3 was set to zero (Supplementary Fig. 10 and Supplementary Table 4). For the three-state static PDA, fit was performed with τ_{ex} set to virtual infinity (>100 ms) for apo and all ligand-bound conditions (Supplementary Fig. 11 and Supplementary Table 5). Criteria for a good fit were a low (<4) global Poissonian χ_{red}^2 value.

In our data, FRET efficiency distributions for MF and HF states are wide and overlapping. Thus, a low-FRET contrast led to a low sensitivity of PDA for dynamics in the data. To test how well our final fFCS-constrained PDA model describes the experimental data compared to the three-state static model, we independently analyzed three datasets, each dataset was obtained from a separate protein aliquot and contained 2000–5000 bursts. We treated these three datasets independently and calculated the mean χ_{red}^2 with SD for fully static and fFCS-constrained models. The static model fitted the reduced datasets with $\chi_{red}^2 = 1.7 \pm 0.1$, while the fFCS-constrained model resulted in $\chi_{red}^2 = 1.9 \pm 0.3$. Therefore, PDA χ_{red}^2 cannot distinguish between the three-state static and fFCS-constrained models.

Fluorescence depolarization measurements. The setup described in “Methods” “Confocal MFD-PIE setup” was used for fluorescence depolarization measurements albeit after improving the temporal resolution of photon detection. Particularly, detectors in the donor channels were replaced with single-photon avalanche diodes (Picoquant MPD PDM-100-CTE, < 25 cps). To preserve the timing resolution, the NIM output of the donor detectors was used. NIM-to-TTL converters (NIM2TTL, Micro Photon Devices) were used to connect NIM outputs of the donor detectors to the photon router (Becker-Hickl HRT82). Measurements were done as described in “Methods” “smFRET data recording”, updated correction factors were applied: $ct = 0.018$, $de = 0.024$, $\gamma = 0.97$, $\beta = 2.1$, $G_B = 0.95$, $G_R = 1.04$. Bursts corresponding to single-labeled molecules were selected. Time-resolved fluorescence anisotropy $r(t)$ was calculated as

$$r(t) = \frac{GF_{||}(t) - F_{\perp}(t)}{GF_{||}(t) + 2F_{\perp}(t)}, \quad (13)$$

where $F_{||}(t)$ is the intensity in the time gate $BB_{||}$ (donor) or $RR_{||}$ (acceptor), and $F_{\perp}(t)$ is the intensity in the time gate BB_{\perp} (donor) or RR_{\perp} (acceptor). Experimental anisotropy decays $r(t)$ (Supplementary Fig. 13) were fitted with a

biexponential model:

$$r(t) = \left((r_0 - r_p) e^{-t/\rho_F} + r_0 \right) e^{-t/\rho_p}. \quad (14)$$

In all cases ρ_p , which describes slow depolarization due to rotation of the protein as a whole, was >50 ns, and therefore affected the fitting process only slightly. Three technical replicas with different protein aliquots were performed, mean and SD values for fitting parameters r_0 (fundamental anisotropy), r_p (residual anisotropy), ρ_F (fluorophore relaxation time) are given in Supplementary Table 7.

Finally, we used a “wobbling-in-a-cone”⁹⁴ model to calculate the typical angular displacement of the fluorophores:

$$\frac{r_p}{r_0^*} = \left(\frac{\cos\theta(1 + \cos\theta)}{2} \right)^2, \quad (15)$$

where $r_0^* = 0.4$ is the fundamental fluorescence of the dyes. We attribute the difference between r_0^* and the observed r_0 to fast rearrangement of the dyes that is not detectable due to the temporal resolution of the apparatus.

Molecular dynamics simulations. The initial model of the $A_{2A}AR$ in the inactive state (amino acids 3–316) embedded in the membrane was prepared using the CHARMM-GUI web-service⁹⁵ based on the structure of a thermostabilized $A_{2A}AR$ in complex with ZM241385 (PDB ID: 3PWH)⁸². The thermostabilized mutations were mutated back to native amino acids and the missing regions were added using MODELLER⁹⁶ with an exception of the loop 212–223, which was omitted to prevent possible interference with the fluorescent label at the position 225 and thus improve its sampling. The structure of $A_{2A}AR$ in complex with mini-Gs (PDB ID 5G53)⁷⁰ including residues 309–312 from the C-terminal linker was used as a template to model the wild-type variant C-terminal residues missing in 3PWH (residues 306–316) and 5G53 (residues 309–316) with residue 310 substituted with a cysteine. The Atto647N-maleimide and Alexa488-C5-maleimide fluorescent labels were attached at the positions 225 and 310 by aligning the backbone atoms of the modified cysteine residues with the bound fluorescent labels to the backbone atoms of corresponding residues of the protein. In total, six simulations were performed: three for each double-labeled variant of $A_{2A}AR$. In these simulations, we used the Atto647N-maleimide dye instead of its derivative Atto643-maleimide used in the experiment, because the structure of the latter was not published. The resulting solvated systems contained 76,765 atoms including 203 POPC lipids, 68 sodium, and 75 chloride ions (labeling variant 1 with Atto647N attached to L225C^{6,27}, and Alexa488 attached to Q310C^{8,65}) and 76,810 atoms including 203 POPC lipids, 68 sodium, and 75 chloride ions (label variant 2 with Alexa488 attached to L225C^{6,27}, and Atto647N attached to Q310C^{8,65}). The simulation boxes had total dimensions of $9.02 \times 9.02 \times 9.20$ nm³ and $9.01 \times 9.01 \times 9.19$ nm³, respectively. All ionizable amino acids were modeled in their standard ionization state at pH 7. The CHARMM-GUI recommended protocol was applied for the initial energy minimization and equilibration of the system. During all of the equilibration steps, the force constants of the harmonic positional restraints on lipids were gradually reduced to zero while those on the protein Ca-atoms were left intact.

The equilibration simulations were followed by targeted MD simulations⁹⁷ in order to steer the systems to the fully active state while inducing minimal effects on the systems. The 5G53 structure was used as a target for targeted simulations to the fully active state. For the targeted MD simulations, the Nose–Hoover thermostat and the Parrinello–Rahman barostat were used. The temperature and pressure were set to 313.3 K and 1 bar with temperature and pressure coupling time constants of 1.0 ps⁻¹ and 0.5 ps⁻¹, respectively. Each targeted simulation was run for 100 ns with the force constant of 50,000 kJ/mol applied to the protein Ca-atoms only.

The triplicate production simulations for the inactive and fully active states were run for 1000 ns in NVT ensemble (maintained by the Nose–Hoover thermostat with $T_{ref} = 313.3$ K, temperature coupling time = 1.0 ps⁻¹) with the protein Ca-atoms constrained by harmonic potentials (1000 kJ/mol/nm²). Each individual simulation was additionally prefaced by a short (10 ns, excluded from the further analysis) equilibration simulation with the random velocities drawn from Maxwell distribution to guarantee the independence of initial conformations. The fluorescent labels were coupled separately to a heat bath ($T_{ref} = 450$ K) to enhance conformational sampling⁹⁸.

All MD simulations were performed by GROMACS version 2020.2⁹⁹ with the PLUMED plugin¹⁰⁰ used for the targeted MD. A time step of 2 fs was used for equilibration simulations except for the early steps (where it was 1 fs), while targeted and production simulations were performed with a 4-fs time step allowed by repartitioning the mass of heavy atoms into the bonded hydrogen atoms¹⁰¹ and the LINCS constraint algorithm¹⁰². The CHARMM36m force field was used for the protein, lipids, and ions¹⁰³. The topologies for the fluorescent labels were obtained using the CGenFF web-service version 1.0.0 (force field version 3.0.1)¹⁰⁴. They are available online as Supplementary Data 3 and Supplementary Data 4.

In order to estimate the convergence of label sampling, we calculated the volume available for each label as a function of simulation time (Supplementary Fig. 16). The estimation was done using the custom script available at https://github.com/porekhov/A2a_smFRET.

All trajectories of the production simulations are available at https://github.com/porekhov/A2a_smFRET.

Burst-wise steady-state fluorescence anisotropies. Burst-wise steady-state fluorescence anisotropies of the donor (r_D) and the acceptor (r_A) were calculated from the respective fluorescence intensities:

$$r = \frac{GF_{\parallel} - F_{\perp}}{GF_{\parallel} + 2F_{\perp}} \quad (16)$$

where G is the correction factor for different detection efficiencies in the two polarization channels ($G_B = 0.99$, $G_R = 1.13$), F_{\parallel} is the intensity in the time gate BB_{\parallel} (donor) or RR_{\parallel} (acceptor), and F_{\perp} is the intensity in the time gate BB_{\perp} (donor) or RR_{\perp} (acceptor).

Statistics and reproducibility. smFRET data were collected for three different protein aliquots and all data derivatives are given as the mean \pm SD. For the cross-correlations fFCS functions, error bars are calculated as SDs obtained after splitting the photon data into ten equally sized bins (Supplementary Fig. 9); the 95% confidence intervals for the fitting parameters were calculated using the numerical Jacobian matrix (Supplementary Table 3). BRET data are collected in three biological replicas and are given as mean \pm SD.

Reporting summary. Further information on research design is available in the Nature Portfolio Reporting Summary linked to this article.

Data availability

All data that support the findings of this study are available from the corresponding author upon reasonable request. The burst data from smFRET experiments and data from molecular dynamics simulations are available in Zenodo with the identifier <https://doi.org/10.5281/zenodo.7722845>¹⁰⁵.

Code availability

All analyses of experimental smFRET data were performed in the software package PAM (PIE Analysis with MATLAB)⁹⁰. The software is available as a source code, requiring MATLAB to run, or as pre-compiled standalone distributions for Windows or MacOS at <http://www.cup.uni-muenchen.de/pc/lamb/software/pam.html> and hosted in Git repositories under <http://www.gitlab.com/PAM-PIE/PAM> and <http://www.gitlab.com/PAM-PIE/PAMcompiled>. A detailed manual is located at <http://pam.readthedocs.io>. The version of PAM used for the analysis of smFRET data is also available in Zenodo with the identifier <https://doi.org/10.5281/zenodo.7722845>¹⁰⁵.

Received: 9 September 2022; Accepted: 17 March 2023;

Published online: 03 April 2023

References

- Kristiansen, K. Molecular mechanisms of ligand binding, signaling, and regulation within the superfamily of G-protein-coupled receptors: molecular modeling and mutagenesis approaches to receptor structure and function. *Pharmacol. Ther.* **103**, 21–80 (2004).
- Gether, U. Uncovering molecular mechanisms involved in activation of G protein-coupled receptors. *Endocrine Rev.* **21**, 90–113 (2000).
- Hauser, A. S., Attwood, M. M., Rask-Andersen, M., Schiöth, H. B. & Gloriam, D. E. Trends in GPCR drug discovery: new agents, targets and indications. *Nat. Rev. Drug Discov.* **16**, 829–842 (2017).
- Seifert, R. & Wenzel-seifert, K. Constitutive activity of G-protein-coupled receptors: cause of disease and common property of wild-type receptors. *Naunyn-Schmiedeberg's Arch. Pharm.* **366**, 381–416 (2002).
- Kenakin, T. Theoretical aspects of GPCR-ligand complex pharmacology. *Chem. Rev.* **117**, 4–20 (2017).
- Smith, J. S., Lefkowitz, R. J. & Rajagopal, S. Biased signalling: from simple switches to allosteric microprocessors. *Nat. Rev. Drug Discov.* **17**, 243–260 (2018).
- Quast, R. B. & Margeat, E. Studying GPCR conformational dynamics by single molecule fluorescence. *Mol. Cell. Endocrinol.* **493**, 110469 (2019).
- Casiraghi, M. et al. NMR analysis of GPCR conformational landscapes and dynamics. *Mol. Cell. Endocrinol.* **484**, 69–77 (2019).
- Gusach, A. et al. Beyond structure: emerging approaches to study GPCR dynamics. *Curr. Opin. Struct. Biol.* **63**, 18–25 (2020).
- Fredholm, B. B., Ijzerman, A. P., Jacobson, K. A., Klotz, K.-N. & Linden, J. International Union of Pharmacology. XXV. Nomenclature and classification of adenosine receptors. *Pharmacol. Rev.* **53**, 527–552 (2001).
- Jacobson, K. A. & Gao, Z. G. Adenosine receptors as therapeutic targets. *Nat. Rev. Drug Discov.* **5**, 247–264 (2006).
- De Lera Ruiz, M., Lim, Y. H. & Zheng, J. Adenosine A2A receptor as a drug discovery target. *J. Med. Chem.* **57**, 3623–3650 (2014).
- Jacobson, K. A., Tosh, D. K., Jain, S. & Gao, Z. G. Historical and current adenosine receptor agonists in preclinical and clinical development. *Front. Cell. Neurosci.* **13**, 1–17 (2019).
- Zezula, J. & Freissmuth, M. The A 2A-adenosine receptor: A GPCR with unique features? *Br. J. Pharm.* **153**, 184–190 (2008).
- Keuerleber, S., Thurner, P., Gruber, C. W., Zezula, J. & Freissmuth, M. Reengineering the collision coupling and diffusion mode of the A 2A-adenosine receptor: palmitoylation in helix 8 relieves confinement. *J. Biol. Chem.* **287**, 42104–42118 (2012).
- Eddy, M. T. et al. Allosteric coupling of drug binding and intracellular signaling in the A2A adenosine receptor. *Cell* **172**, 68–80.e12 (2018).
- Eddy, M. T. et al. Extrinsic tryptophans as NMR probes of allosteric coupling in membrane proteins: application to the A2A adenosine receptor. *J. Am. Chem. Soc.* **140**, 8228–8235 (2018).
- Clark, L. D. et al. Ligand modulation of sidechain dynamics in a wild-type human GPCR. *eLife* **6**, 1–27 (2017).
- Ye, L. et al. Activation of the A2A adenosine G-protein-coupled receptor by conformational selection. *Nature* **533**, 265–268 (2016).
- Mizumura, T. et al. Activation of adenosine A2A receptor by lipids from docosahexaenoic acid revealed by NMR. *Sci. Adv.* **6**, 1–15 (2020).
- Sušac, L., Eddy, M. T., Didenko, T., Stevens, R. C. & Wüthrich, K. A 2A adenosine receptor functional states characterized by 19 F-NMR. *Proc. Natl Acad. Sci. USA* **115**, 12733–12738 (2018).
- Ye, L. et al. Mechanistic insights into allosteric regulation of the A2A adenosine G protein-coupled receptor by physiological cations. *Nat. Commun.* **9**, 1–13 (2018).
- Huang, S. K. et al. Delineating the conformational landscape of the adenosine A 2A receptor during G protein coupling. *Cell* **184**, 1–11 (2021).
- Eddy, M. T., Martin, B. T. & Wüthrich, K. A2A adenosine receptor partial agonism related to structural rearrangements in an activation microswitch. *Structure* **29**, 170–176.e3 (2021).
- Lerner, E. et al. FRET-based dynamic structural biology: challenges, perspectives and an appeal for open-science practices. *eLife* **10**, e60416 (2021).
- Peleg, G., Ghanouni, P., Kobilka, B. K. & Zare, R. N. Single-molecule spectroscopy of the β_2 adrenergic receptor: observation of conformational substates in a membrane protein. *Proc. Natl Acad. Sci. USA* **98**, 8469–8474 (2001).
- Bockenbauer, S., Fürstenberg, A., Yao, X. J., Kobilka, B. K. & Moerner, W. E. Conformational dynamics of single G protein-coupled receptors in solution. *J. Phys. Chem. B* **115**, 13328–13338 (2011).
- Lamichhane, R. et al. Single-molecule view of basal activity and activation mechanisms of the G protein-coupled receptor β_2 AR. *Proc. Natl Acad. Sci. USA* **112**, 14254–14259 (2015).
- Lamichhane, R. et al. Biased signaling of the G-protein-coupled receptor β_2 AR is governed by conformational exchange kinetics. *Structure* **28**, 371–377.e3 (2020).
- Maeda, R. et al. Single-molecule observation of the ligand-induced population shift of rhodopsin, A G-protein-coupled receptor. *Biophys. J.* **106**, 915–924 (2014).
- Maeda, R. et al. Shift in conformational equilibrium induces constitutive activity of G-protein coupled receptor, rhodopsin. *J. Phys. Chem. B* **122**, 4838–4843 (2018).
- Wei, S. et al. Slow conformational dynamics of the human A2A adenosine receptor are temporally ordered. *Structure* **30**, 329–337.e5 (2022).
- Olofsson, L. et al. Fine tuning of sub-millisecond conformational dynamics controls metabotropic glutamate receptors agonist efficacy. *Nat. Commun.* **5**, 1–12 (2014).
- Vafabakhsh, R., Levitz, J. & Isacoff, E. Y. Conformational dynamics of a class C G-protein-coupled receptor. *Nature* **524**, 497–501 (2015).
- Dijkman, P. M. et al. Dynamic tuneable G protein-coupled receptor monomer-dimer populations. *Nat. Commun.* **9**, 1–14 (2018).
- Habrian, C. H. et al. Conformational pathway provides unique sensitivity to a synaptic mGluR. *Nat. Commun.* **10**, 1–13 (2019).
- Walsh, S. M. et al. Single proteoliposome high content analysis reveals differences in the homo-oligomerization of GPCRs. *Biophys. J.* **115**, 300–312 (2018).
- Gregorio, G. G. et al. Single-molecule analysis of ligand efficacy in β_2 AR-G-protein activation. *Nature* **547**, 68–73 (2017).
- Kudryavtsev, V. et al. Combining MFD and PIE for accurate single-pair Förster resonance energy transfer measurements. *ChemPhysChem* **13**, 1060–1078 (2012).
- Ballesteros, J. A. & Weinstein, H. Integrated methods for the construction of three-dimensional models and computational probing of structure-function relations in G protein-coupled receptors. *Methods Neurosci.* **25**, 366–428 (1995).

41. Kalinin, S., Valeri, A., Antonik, M., Felekyan, S. & Seidel, C. A. M. Detection of structural dynamics by FRET: a photon distribution and fluorescence lifetime analysis of systems with multiple states. *J. Phys. Chem. B* **114**, 7983–7995 (2010).
42. Tomov, T. E. et al. Disentangling subpopulations in single-molecule FRET and ALEX experiments with photon distribution analysis. *Biophys. J.* **102**, 1163–1173 (2012).
43. Torella, J. P., Holden, S. J., Santoso, Y., Hohlbein, J. & Kapanidis, A. N. Identifying molecular dynamics in single-molecule FRET experiments with burst variance analysis. *Biophys. J.* **100**, 1568–1577 (2011).
44. Felekyan, S., Kalinin, S., Valeri, A. & Seidel, C. A. M. Filtered FCS and species cross correlation function. *Multiphoton Microsc. Biomed. Sci.* **IX** 7183, 71830D (2009).
45. Hoffmann, C. et al. A FAsH-based FRET approach to determine G protein-coupled receptor activation in living cells. *Nat. Methods* **2**, 171–176 (2005).
46. Fernández-Dueñas, V. et al. Uncovering caffeine's adenosine A2A receptor inverse agonism in experimental parkinsonism. *ACS Chem. Biol.* **9**, 2496–2501 (2014).
47. Ghanouni, P. et al. Functionally different agonists induce distinct conformations in the G protein coupling domain of the β_2 adrenergic receptor. *J. Biol. Chem.* **276**, 24433–24436 (2001).
48. Ghanouni, P., Steenhuis, J. J., Farrens, D. L. & Kobilka, B. K. Agonist-induced conformational changes in the G-protein-coupling domain of the β_2 adrenergic receptor. *Proc. Natl Acad. Sci. USA* **98**, 5997–6002 (2001).
49. Cohen, B. E. et al. A fluorescent probe designed for studying protein conformational change. *Proc. Natl Acad. Sci. USA* **102**, 965–970 (2005).
50. Swaminath, G. et al. Sequential binding of agonists to the β_2 adrenoceptor: kinetic evidence for intermediate conformational states. *J. Biol. Chem.* **279**, 686–691 (2004).
51. Swaminath, G. et al. Probing the β_2 adrenoceptor binding site with catechol reveals differences in binding and activation by agonists and partial agonists. *J. Biol. Chem.* **280**, 22165–22171 (2005).
52. Sušac, L., O'Connor, C., Stevens, R. C. & Wütrich, K. In-membrane chemical modification (IMCM) for site-specific chromophore labeling of GPCRs. *Angew. Chem. Int. Ed.* **54**, 15246–15249 (2015).
53. Denisov, I. G., Grinkova, Y. V., Lazarides, A. A. & Sligar, S. G. Directed self-assembly of monodisperse phospholipid bilayer nanodiscs with controlled size. *J. Am. Chem. Soc.* **126**, 3477–3487 (2004).
54. Alexandrov, A. I., Mileni, M., Chien, E. Y. T., Hanson, M. A. & Stevens, R. C. Microscale fluorescent thermal stability assay for membrane proteins. *Structure* **16**, 351–359 (2008).
55. Middleton, R. J. et al. New fluorescent adenosine A₁-receptor agonists that allow quantification of ligand–receptor interactions in microdomains of single living cells. *J. Med. Chem.* **50**, 782–793 (2007).
56. van Tilburg, E. W., von Kunzel, J. F. D., De Groote, M. & Ijzerman, A. P. 2, 5'-disubstituted adenosine derivatives: evaluation of selectivity and efficacy for the adenosine A₁, A_{2A}, and A₃ receptor. *J. Med. Chem.* **45**, 420–429 (2002).
57. Bosch, M. P. et al. Synthesis and biological activity of new potential agonists for the human adenosine A_{2A} receptor. *J. Med. Chem.* **47**, 4041–4053 (2004).
58. Knight, A. et al. Discovery of novel adenosine receptor agonists that exhibit subtype selectivity. *J. Med. Chem.* 947–964 (2016).
59. Olah, M. E. Identification of A_{2A} adenosine receptor domains involved in selective coupling to Gs: analysis of chimeric A₁/A_{2A} adenosine receptors. *J. Biol. Chem.* **272**, 337–344 (1997).
60. Müller, B. K., Zaychikov, E., Bräuchle, C. & Lamb, D. C. Pulsed interleaved excitation. *Biophys. J.* **89**, 3508–3522 (2005).
61. Widengren, J. et al. Single-molecule detection and identification of multiple species by multiparameter fluorescence detection. *Anal. Chem.* **78**, 2039–2050 (2006).
62. Antonik, M., Felekyan, S., Gaiduk, A. & Seidel, C. A. M. Separating structural heterogeneities from stochastic variations in fluorescence resonance energy transfer distributions via photon distribution analysis. *J. Phys. Chem. B* **110**, 6970–6978 (2006).
63. Nir, E. et al. Shot-noise limited single-molecule FRET histograms: comparison between theory and experiments. *J. Phys. Chem. B* **110**, 22103–22124 (2006).
64. Chung, K. Y. et al. Role of detergents in conformational exchange of a G protein-coupled receptor. *J. Biol. Chem.* **287**, 36305–36311 (2012).
65. Kofuku, Y. et al. Functional dynamics of deuterated β_2 -adrenergic receptor in lipid bilayers revealed by NMR spectroscopy. *Angew. Chem. Int. Ed.* **53**, 13376–13379 (2014).
66. Fernandes, D. D. et al. Ligand modulation of the conformational dynamics of the A_{2A} adenosine receptor revealed by single-molecule fluorescence. *Sci. Rep.* **11**, 5910 (2021).
67. Xu, F. et al. Structure of an agonist-bound human A_{2A} adenosine receptor. *Science* **332**, 322–327 (2011).
68. Lebon, G. et al. Agonist-bound adenosine A_{2A} receptor structures reveal common features of GPCR activation. *Nature* **474**, 521–526 (2011).
69. Jaakola, V. P. et al. The 2.6 angstrom crystal structure of a human A_{2A} adenosine receptor bound to an antagonist. *Science* **322**, 1211–1217 (2008).
70. Carpenter, B., Nehmé, R., Warne, T., Andrew, G. W. & Tate, C. G. Structure of the adenosine A_{2A} receptor bound to an engineered G protein. *Nature* **536**, 104–107 (2016).
71. Bostock, M. J., Solt, A. S. & Nietlispach, D. The role of NMR spectroscopy in mapping the conformational landscape of GPCRs. *Curr. Opin. Struct. Biol.* **57**, 145–156 (2019).
72. Seidel, M. G., Klinger, M., Freissmuth, M. & Höller, C. Activation of mitogen-activated protein kinase by the A_{2A}-adenosine receptor via a rap1-dependent and via a p21ras-dependent pathway. *J. Biol. Chem.* **274**, 25833–25841 (1999).
73. Bennett, K. A. et al. Pharmacology and structure of isolated conformations of the adenosine A_{2A} receptor define ligand efficacy. *Mol. Pharmacol.* **83**, 949–958 (2013).
74. Massink, A. et al. Sodium ion binding pocket mutations and adenosine A_{2A} receptor function. *Mol. Pharmacol.* **87**, 305–313 (2015).
75. Klinger, M. et al. Removal of the carboxy terminus of the A_{2A}-adenosine receptor blunts constitutive activity: Differential effect on cAMP accumulation and MAP kinase stimulation. *Naunyn. Schmiedeberg's Arch. Pharmacol.* **366**, 287–298 (2002).
76. Welihinda, A. A., Kaur, M., Greene, K., Zhai, Y. & Amento, E. P. The adenosine metabolite inosine is a functional agonist of the adenosine A_{2A} receptor with a unique signaling bias. *Cell. Signal.* **28**, 552–560 (2016).
77. Bertheleme, N., Singh, S., Dowell, S. J., Hubbard, J. & Byrne, B. Loss of constitutive activity is correlated with increased thermostability of the human adenosine A_{2A} receptor. *Br. J. Pharmacol.* **169**, 988–998 (2013).
78. McGraw, C. et al. Membrane cholesterol depletion reduces downstream signaling activity of the adenosine A_{2A} receptor. *Biochim. Biophys. Acta - Biomembr.* **1861**, 760–767 (2019).
79. Lebon, G., Edwards, P. C., Leslie, A. G. W. & Tate, C. G. Molecular determinants of CGS21680 binding to the human adenosine A_{2A} receptor. *Mol. Pharmacol.* **87**, 907–915 (2015).
80. Zhang, Z. H. et al. Expression of a short antibody heavy chain peptide effectively antagonizes adenosine A_{2A} receptor in vitro and in vivo. *Expert Opin. Ther. Targets* **24**, 707–717 (2020).
81. Guo, D. et al. Binding kinetics of ZM241385 derivatives at the human adenosine A_{2A} receptor. *ChemMedChem* **9**, 752–761 (2014).
82. Doré, A. S. et al. Structure of the adenosine A_{2A} receptor in complex with ZM241385 and the xanthines XAC and caffeine. *Structure* **19**, 1283–1293 (2011).
83. Bayburt, T. H., Grinkova, Y. V. & Sligar, S. G. Self-assembly of discoidal phospholipid bilayer nanoparticles with membrane scaffold proteins. *Nano Lett.* **2**, 853–856 (2002).
84. Geiger, A. et al. Correlating calcium binding, foerster resonance energy transfer, and conformational change in the biosensor TN-XXL. *Biophys. J.* **102**, 2401–2410 (2012).
85. Pandey, S., Roy, D. & Shukla, A. K. Measuring surface expression and endocytosis of GPCRs using whole-cell ELISA. in *G Protein-Coupled Receptors Part B* (ed. Shukla, A. K.) Vol. 149, 131–140 (Elsevier Inc., 2018).
86. Salahpour, A. et al. BRET biosensors to study GPCR biology, pharmacology, and signal transduction. *Front. Endocrinol.* **3**, 1–10 (2012).
87. Barak, L. S. et al. Pharmacological characterization of membrane-expressed human trace amine-associated receptor 1 (TAAR1) by a bioluminescence resonance energy transfer cAMP biosensor. *Mol. Pharmacol.* **74**, 585–594 (2008).
88. Vandenberk, N., Barth, A., Borrenberghs, D., Hofkens, J. & Hendrix, J. Evaluation of blue and far-red dye pairs in single-molecule Förster resonance energy transfer experiments. *J. Phys. Chem. B* **122**, 4249–4266 (2018).
89. Schaffer, J. et al. Identification of single molecules in aqueous solution by time-resolved fluorescence. *J. Phys. Chem. A* **103**, 331–336 (1999).
90. Schrimpf, W., Barth, A., Hendrix, J. & Lamb, D. C. PAM: a framework for integrated analysis of imaging, single-molecule, and ensemble fluorescence data. *Biophys. J.* **114**, 1518–1528 (2018).
91. Lee, N. K. et al. Accurate FRET measurements within single diffusing biomolecules using alternating-laser excitation. *Biophys. J.* **88**, 2939–2953 (2005).
92. Felekyan, S., Kalinin, S., Sanabria, H., Valeri, A. & Seidel, C. A. M. Filtered FCS: species auto- and cross-correlation functions highlight binding and dynamics in biomolecules. *ChemPhysChem* **13**, 1036–1053 (2012).
93. Sisamakia, E., Valeri, A., Kalinin, S., Rothwell, P. J. & Seidel, C. A. M. *Accurate Single-Molecule FRET Studies Using Multiparameter Fluorescence Detection. Single Molecule Tools, Part B: Super-Resolution, Particle Tracking, Multiparameter, and Force Based Methods* Vol. 475 (Elsevier Inc., 2010).
94. Kinoshita, K., Ikegami, A. & Kawato, S. On the wobbling-in-cone analysis of fluorescence anisotropy decay. *Biophys. J.* **37**, 461–464 (1982).
95. Jo, S., Kim, T., Iyer, V. G. & Im, W. Software news and updates CHARMM-GUI: a web-based graphical user interface for CHARMM. *J. Comput. Chem.* **29**, 1859–1865 (2008).
96. Webb, B. & Sali, A. Comparative protein structure modeling using MODELLER. *Curr. Protoc. Bioinform.* **54**, 1–37 (2016).

97. Schlitter, J. Targeted molecular dynamics: a new approach for searching pathways of conformational transitions. *J. Mol. Graph.* **12**, 84–89 (1994).
98. Klose, D., Klare, J. P., Grohmann, D., Kay, C. W. M. & Werner, F. Simulation vs. reality: a comparison of in silico distance predictions with DEER and FRET measurements. *PLoS ONE* **7**, e39492 (2012).
99. Abraham, J. M. et al. GROMACS: high performance molecular simulations through multi-level parallelism from laptops to supercomputers. *SoftwareX* **1–2**, 19–25 (2015).
100. Bussi, G. & Tribello, G. A. Analyzing and biasing simulations with PLUMED. in *Biomolecular Simulations* (eds Bonomi, M. & Camilloni, C.) 529–578 (Springer, 2019).
101. Hopkins, C. W., Grand, S. Le., Walker, R. C. & Roitberg, A. E. Long-time-step molecular dynamics through hydrogen mass repartitioning. *J. Chem. Theory Comput.* **11**, 1864–1874 (2015).
102. Hess, B., Bekker, H., Berendsen, H. J. C. & Fraaije, J. G. E. M. LINCS: a linear constraint solver for molecular simulations. *J. Comput. Chem.* **18**, 1463–1472 (1997).
103. Huang, J. et al. CHARMM36m: an improved force field for folded and intrinsically disordered proteins. *Nat. Methods* **14**, 71–73 (2017).
104. Vanommeslaeghe, K. et al. CHARMM general force field: a force field for drug-like molecules compatible with the CHARMM all-atom additive biological force fields. *J. Comput. Chem.* **31**, 671–690 (2010).
105. Maslov, I. et al. Supplementary materials for ‘Sub-millisecond conformational dynamics of the A2A adenosine receptor revealed by single-molecule FRET’. *Zenodo* <https://doi.org/10.5281/zenodo.7722845> (2023).
106. Kalinin, S. et al. A toolkit and benchmark study for FRET-restrained high-precision structural modeling. *Nat. Methods* **9**, 1218–1225 (2012).
107. Lomize, M. A., Pogozheva, I. D., Joo, H., Mosberg, H. I. & Lomize, A. L. OPM database and PPM web server: resources for positioning of proteins in membranes. *Nucleic Acids Res.* **40**, 370–376 (2012).

Acknowledgements

A.L., A.B., and V.B. are thankful for the Ministry of Science and Higher Education of the Russian Federation (agreement #075-03-2023-106, project FSMG-2020-0003). IM acknowledges the UHasselt Special Research Fund. Measurements of surface expression and Gs-signaling were supported by the Russian Science Foundation (project no. 22-74-10036; <https://rscf.ru/project/22-74-10036/>). Computational simulations were supported by the National Natural Science Foundation of China, grant #32250410316 (to PO). We acknowledge the Advanced Optical Microscopy Centre at Hasselt University for support with microscopy experiments. Microscopy was made possible by the Research Foundation Flanders (FWO), projects G0B4915, G0B9922N, and G0H3716N).

Author contributions

O.V. performed receptor expression. I.M. and O.V. performed receptor labeling, purification, and nanodisc reconstitution. T.G. and I.M. performed ensemble-TCSPC

measurements. I.M. and Q.C. measured fluorescence spectra. Q.C. and J.He. prepared the instrumentation for smFRET experiments. I.M. performed smFRET experiments, analyzed smFRET data and drafted the manuscript. J.He., A.Ba., S.W., A.Bo., and V.B. contributed to the analysis of smFRET data. A.Ge. performed cell functional assay. P.Kh performed TSA functional assay with the contribution of A.M., A.L., A.Gu., and P.Ku. P.O. performed molecular dynamics simulations. I.M., V.B., J.He., V.C., T.G., A.Bo., A.Gu., A.M., P.Kh., and V.G. discussed the data, analysis, and contributed to writing the manuscript. I.M., V.B., J.He., V.C., T.G., and J.Ho. conceived the study. All authors commented on and edited the manuscript. V.B. and J.He. supervised the project.

Competing interests

The authors declare no competing interests.

Additional information

Supplementary information The online version contains supplementary material available at <https://doi.org/10.1038/s42003-023-04727-z>.

Correspondence and requests for materials should be addressed to Jelle Hendrix or Valentin Borshchevskiy.

Peer review information *Communications Biology* thanks the anonymous reviewers for their contribution to the peer review of this work. Primary Handling Editors: Ross Bathgate and Gene Chong. Peer reviewer reports are available.

Reprints and permission information is available at <http://www.nature.com/reprints>

Publisher's note Springer Nature remains neutral with regard to jurisdictional claims in published maps and institutional affiliations.



Open Access This article is licensed under a Creative Commons Attribution 4.0 International License, which permits use, sharing, adaptation, distribution and reproduction in any medium or format, as long as you give appropriate credit to the original author(s) and the source, provide a link to the Creative Commons license, and indicate if changes were made. The images or other third party material in this article are included in the article's Creative Commons license, unless indicated otherwise in a credit line to the material. If material is not included in the article's Creative Commons license and your intended use is not permitted by statutory regulation or exceeds the permitted use, you will need to obtain permission directly from the copyright holder. To view a copy of this license, visit <http://creativecommons.org/licenses/by/4.0/>.

© The Author(s) 2023